Research Article

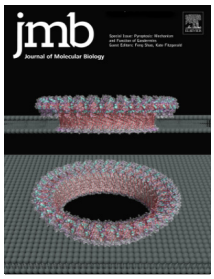

Protein Allostery and Ligand Design: Computational Design Meets Experiments to Discover Novel Chemical Probes

Alice Triveri [1,†], Carlos Sanchez-Martin [2,†], Luca Torielli [1,†], Stefano A. Serapian [1], Filippo Marchetti [1], Giovanni D'Acerno [1], Valentina Pirota [1], Matteo Castelli [1], Elisabetta Moroni [3], Mariarosaria Ferraro [3], Paolo Quadrelli [1,*], Andrea Rasola [2,*] and Giorgio Colombo [1,3,*]

*1 - **University of Pavia,** Department of Chemistry, Via Taramelli 12, 27100 Pavia, Italy*
*2 - **University of Padova,** Department of Biomedical Sciences, Viale G. Colombo 3, 35131 Padova, Italy*
*3 - **Istituto di Scienze e Tecnologie Chimiche "Giulio Natta" – SCITEC CNR,** Via Mario Bianco 9, 20131 Milano, Italy*

Correspondence to Paolo Quadrelli, Andrea Rasola and Giorgio Colombo: University of Pavia, Department of Chemistry, Via Taramelli 12, 27100 Pavia, Italy (G. Colombo, P. Quadrelli); University of Padova, Department of Biomedical Sciences, Viale G. Colombo 3, 35131 Padova, Italy (A. Rasola). *paolo.quadrelli@unipv.it (P. Quadrelli), andrea.rasola@unipd.it (A. Rasola), g.colombo@unipv.it (G. Colombo), @arasola (A. Rasola), @lab_colombo (G. Colombo)*

https://doi.org/10.1016/j.jmb.2022.167468
Edited by Igor N. Berezovsky

Abstract

Herein we examine the determinants of the allosteric inhibition of the mitochondrial chaperone TRAP1 by a small molecule ligand. The knowledge generated is harnessed into the design of novel derivatives with interesting biological properties. TRAP1 is a member of the Hsp90 family of proteins, which work through sequential steps of ATP processing coupled to client-protein remodeling. Isoform selective inhibition of TRAP1 can provide novel information on the biomolecular mechanisms of molecular chaperones, as well as new insights into the development of small molecules with therapeutic potential. Our analysis of the interactions between an active first-generation allosteric ligand and TRAP1 shows how the small molecule induces long-range perturbations that influence the attainment of reactive poses in the active site. At the same time, the dynamic adaptation of the allosteric binding pocket to the presence of the first-generation compound sets the stage for the design of a set of second-generation ligands: the characterization of the formation/disappearance of pockets around the allosteric site that is used to guide optimize the ligands' fit for the allosteric site and improve inhibitory activities. The effects of the newly designed molecules are validated experimentally *in vitro* and *in vivo*. We discuss the implications of our approach as a promising strategy towards understanding the molecular determinants of allosteric regulation in chemical and molecular biology, and towards speeding up the design of allosteric small molecule modulators.

Introduction

Allostery in all its aspects plays fundamental roles in biological function and dysfunction.

Allostery at large can be defined as the property of biomolecules to undergo a modulation of activity or affinity at a primary active site caused by an "effector" at a different distant position, called the allosteric site.[1,2] The effector can be a covalent modification, a mutation, or a ligand. The end result is a perturbation of the biomolecule's functionally-oriented structural dynamics, causing increase or decrease of its activity and, eventually, downstream effects in the cell. Allostery is thus

Please cite tts article as: A. Triveri, C. Sanchez-Martin, L. Torielli, et al., Protein Allostery and Ligand Design: Computational Design Meets Experiments to Discover Novel Chemical ProbesJournal of Molecular Biology, https://doi.org/10.1016/j.jmb.2022.167468

one of the most powerful means to regulate biological systems.[3–5]

As a consequence, our ability to understand and control allostery can have profound implications in both fundamental and applicative research. From the fundamental point of view, the investigation of allostery at different levels, from protein structure and dynamics to interaction networks and systems regulation, can help in understanding how complex biosystems control the mechanisms of intricate biochemical pathways.[4,6] These efforts can further our knowledge of the molecular basis of cell-life.

From the practical point of view, understanding allostery can provide new opportunities in the biotechnological realm, from the regulation of enzyme activity for industrial applications to the development of biomedical solutions, such as allosteric therapeutics.[7,8]

The integration of computational/theoretical methods with chemical design and molecular biology has the potential to advance atomic level mechanistic understanding of the role of protein structure and dynamics into new design rules for the development of modulators of signaling pathways.[4,9–13] In this framework, the validity of computational models describing how an allosteric signal is wired through a protein can be assessed by our ability to design molecules able to induce desired perturbations in the protein activity and, at larger scale, at the cellular level. This would open the possibility to develop optimized allosteric ligands, expanding the arsenal of functional modulators.

The key challenge consists in identifying privileged structures capable of selectively interfering with key functional allosteric residues and sub-states of the target protein. If the target represents a central regulator of networks underlying important signaling pathways, the effect of the allosteric ligand would expectedly reverberate on entire signaling cascades important for cell life.[13–22]

To progress along this path, here we investigate computationally the dynamic cross-talk between an active first-generation allosteric lead and its intended target protein and use this information for the evolution of second-generation ligands. The design is integrated with biochemical and cell biology activity tests. Our goal is to harness our understanding of biomolecular interactions and dynamics to increase the efficiency with which appropriate chemical modulators of signaling pathways can be identified.

As a test system, we focus on the chaperone protein TRAP1, the mitochondrial isoform of the Hsp90 family of molecular chaperones. Hsp90 in humans consists of four ATPase driven isoforms (TRAP1 in mitochondria, Hsp90α and Hsp90β in the cytosol, Grp94 in the endoplasmic reticulum).[23,24] They all share a homodimeric organization, with each protomer consisting of three structural domains: an N-terminal regulatory Domain (NTD), responsible for ATP binding, a Middle Domain (M−domain) which completes the ATPase site necessary for ATP hydrolysis and hosts the binding site for client proteins, and a C-terminal Domain (CTD) involved in dimerization.[23,25,26]

Biochemical and structural studies have led to a general mechanistic model in which global conformational modulations are triggered by ATP: ATP binding at the N-terminal Domain[27] shifts the chaperone to a partially closed, and then into an asymmetric closed conformation that is significantly strained at the Middle:CTD interface, the region involved in client binding.[28] Upon ATP hydrolysis, strain is relieved through rearrangement of the client binding-site residues, driving structural changes in the client. In this framework, ATP hydrolysis is coupled to client remodeling. Specific to TRAP1 3D structure is the peculiar structural asymmetry consisting of a straight and a buckled protomer (Figure 1(a)). The asymmetry is indeed due to buckling of a helix in the M−Domain largely coinciding with the client binding site. Data from the Agard Lab show that this asymmetry sets up differential hydrolysis rates for each protomer, such that the buckled conformation favors ATP hydrolysis, defining a direct coupling of ATP hydrolysis and the client-binding site.[29]

The chaperoning roles of different Hsp90 paralogs are non-overlapping.[30] As a consequence, the development of molecules that permit the selective perturbation of a specific-isoform activity are of crucial interest for pharmacology, with the discovery of new potential drugs, but also for chemical biology at large, with specific ligands acting as chemical tools to address the functions of the protein in its unmodified environment.[31,32]

In this context, the investigation of allosteric mechanisms provides a solid basis for innovation.[33–39] In contrast to orthosteric Hsp90-family inhibitors, allosteric ligands do not need to overcome competition with the abundant endogenous ATP, thus potentially permitting lower dosages than the ones known to determine detrimental effects in classic Hsp90 active site directed drugs. Moreover, allosteric sites tend to be under lower conservation pressure, which can facilitate the design of more specific isoform-targeting drugs and potentially reduce the risks of toxicity or side-effects.[37–49] Sequence variations can influence structural and conformational dynamics traits that are markedly different among paralogs.

This is particularly relevant in the case of TRAP1, a key regulator of mitochondrial homeostasis with roles in diverse pathologic states. TRAP1 regulates proteins such as succinate dehydrogenase (SDH), ERK kinases, Cyclophilin-D (CyP-D), and F-ATP synthase,[50] all of which are involved in tumor cell development and survival.

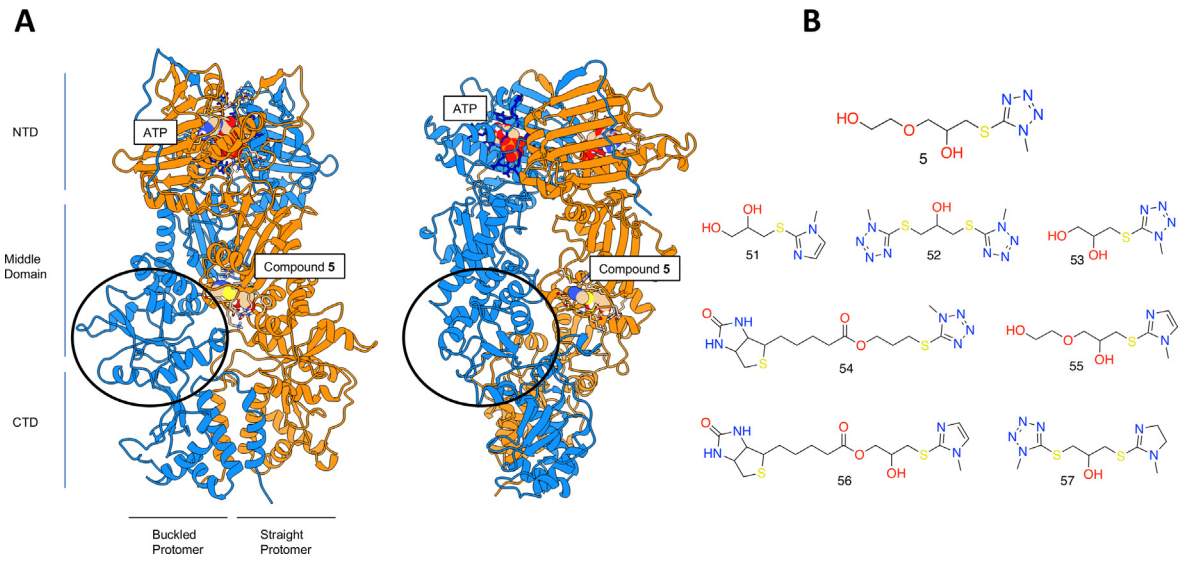

Figure 1. Structures of TRAP1 and Allosteric Compound 5. **A.** Three dimensional structure of TRAP1 with 2 ATP molecules bound at the N-terminal domain, and compound **5** bound at the Middle domain of the straight protomer. The two protomers are colored differently: blue, buckled; orange, straight. The buckled region is highlighted with a circle. **B.** The molecular structure of compound **5** and of the derivatives designed starting from **5.**

TRAP1 overexpression is associated with several tumor types, including prostate, breast and neurofibromatosis NF1 cancer.[51–53] In spite of these observations, induction of TRAP1 levels is somewhat disputed in certain tumor settings, such as kidney cancer.[54,55]

These data highlight the complex and only partially understood role of TRAP1 in cancer progression and underline the necessity for specific targeting of its activities. Up to now, TRAP1 studies have largely relied on cell models where TRAP1 expression was ablated. While informative, this approach is limited, as observed effects originate from engineered cells where non-natural biochemical responses linked to protein ablation could also be induced.

Building on these considerations, we previously developed computational approaches to investigate long-range allosteric communication mechanisms in TRAP1. We identified specific TRAP1 substructures, different from the ones in Hsp90 homologues, that are allosterically connected to the ATP-site.[56] In particular, the presence of ATP in the N-terminal domains resulted in a buildup of strain *only* in the TRAP1 substructure of the straight protomer which is reconfigured at the Middle:CTD interface,[36] and not in Hsp90. The characterization of the steric and electrostatic properties was used to develop complementary pharmacophore models for drug-screening. The resulting identified small molecules proved able to inhibit TRAP1 ATPase while leaving Hsp90 unscathed and revert TRAP1-dependent downregulation of SDH activity in cancer cells. Interestingly, this isoform selectivity could not be achieved by targeting the ATPase binding site, which is highly conserved among paralogs. One inhibitor in particular, named **compound 5** in[36] and shown in Figure 1(b), besides acting as a genuine allosteric inhibitor of ATPase, turned out to show interesting anticancer activities *in vivo*.

In this paper, we set out to combine the characterization of the structural dynamic cross-talk between TRAP1 and the lead **compound 5**,[36] with the design and experimental validation of second-generation allosteric ligands that can selectively perturb the functional mechanisms of TRAP1.

Results

In our previous paper,[36] we characterized the salient structural traits of TRAP1 binding and the biological effects of **5**. The lead was modeled to bind the pocket in the M−Domain of the straight protomer characterized by the presence of residues that are highly coordinated to the ATP-binding site as described in.[36,56]

The effects of the allosteric ligand on the global and internal dynamics of TRAP1. To characterize the effects of **5** on the functionally-oriented motions of TRAP1, we systematically analyzed the outcome molecular dynamics simulations (MD) of the chaperone in the absence (henceforth [2 ATP]) *versus* presence of **5** (henceforth [2ATP + **5**]): five independent MD replicas were carried out for each of the two systems (see *Methods* section). Namely, we combined principal components analysis of MD trajectories with the analysis of internal coordination patterns, in the presence and absence of the allosteric ligand.

To characterize the effects of **5** on the functionally-oriented motions of TRAP1, we combined Principal Components Analysis of MD trajectories,[57] which allows to emphasize the amplitude and directions of dominant protein motions, with the analysis of internal coordination patterns, in the presence and absence of the allosteric ligand.

Figure 2(a) and (b) illustrates the outcome of principal component analysis on our concatenated MD trajectories (metatrajectories, 2.5 μs per system) of [2 ATP] and [2 ATP + **5**] (see *Methods* section): in the top left and right panels, we plot the projection of [2 ATP] and [2 ATP + **5**] metatrajectories, respectively, onto the first (PC 1) and second (PC 2) principal components obtained from trajectory [2 ATP]. Conversely, plots in the bottom panel show metatrajectories of [2 ATP] and [2 ATP + **5**] projected onto the PC 1 and PC 2 of [2 ATP + **5**].

At identical scales, it is clear that binding of **5** to TRAP1 has significant repercussions on the nature of its slower conformational motions. First, the main principal components are different. Moreover, when projected onto PC 1 and PC 2 of [2 ATP] trajectories, [2 ATP + **5**] (top right) is seen to span a more compact and restricted space compared to [2 ATP] (top left), indicating that comparable motions are less prominent. On the other hand, [2 ATP + **5**]'s movement is seen to be more prominent along its own two principal components compared to [2 ATP], again confirming, from a different perspective, that removal of **5** significantly alters the nature of TRAP1's slower conformational motions.

Next, to address in more detail how the binding of **5** can influence the relevant traits of internal dynamics that eventually result in different large-scale motions, we characterized the common and differential patterns in the fluctuations of pairwise amino acid distances from the comparative analysis of [2 ATP] and [2 ATP + **5**] metatrajectories. For each metatrajectory, the pairwise mean-square distance fluctuations are shown in the color-coded matrices of Figure 3(a). The parameter reported in the matrices is called Distance Fluctuation, DF (See *Methods*).[58–61]

From a general point of view, the two DF matrices exhibit a similar "block" character, reflecting the alternation of regions with small and large fluctuations of inter-residue distances in line with the tripartite domain organization of each protomer (N-terminal, Middle, C-terminal; Figure 3(a)). However, in depth analysis of the matrices shows that the DFs of residues belonging to different

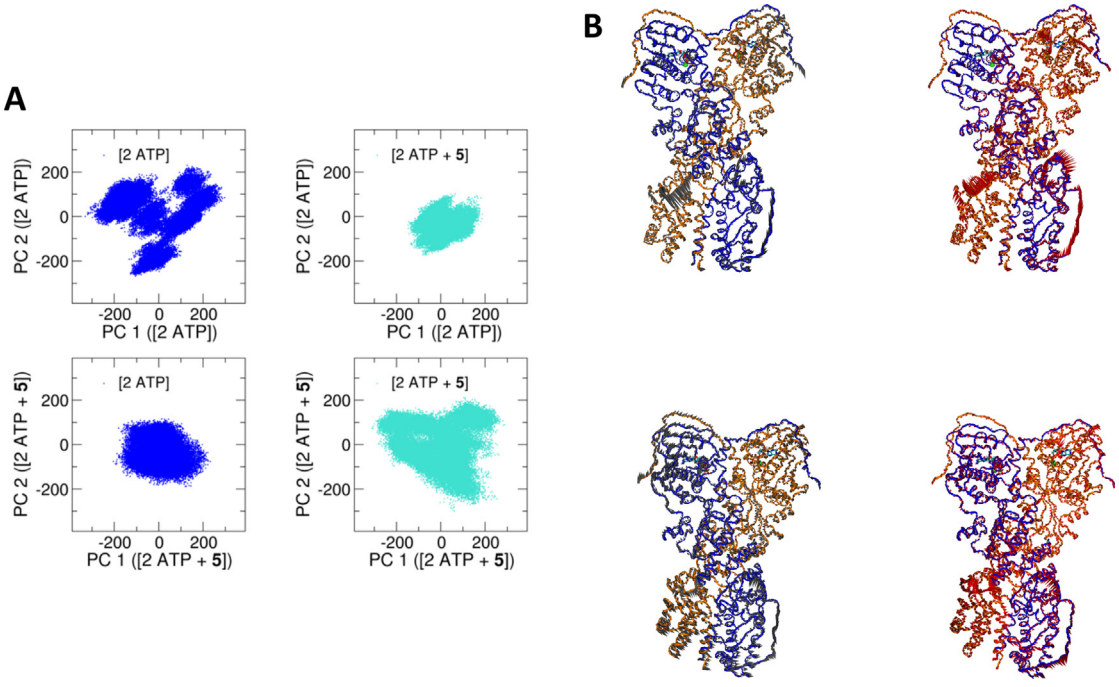

Figure 2. The Slow Motions of TRAP1 Are Influenced by Compound 5. **A.** Principal component analysis. Combined MD simulations of [2 ATP] (blue plots) and [2 ATP + **5**] (cyan plots) are projected frame-by-frame both onto the first two principal components (PC 1 and PC 2) of [2 ATP] (top plots) and [2 ATP + **5**] (bottom plots). **B.** Porcupine plots of PC 1 (grey) and PC 2 (red) superimposed on the average structures of [2 ATP] (top two panels) and [2 ATP + **5**] bottom two panels), viewed from similar perspectives. The buckled protomer is rendered in blue, the straight in orange. ATP molecules (and 5, where present) are rendered as sticks, Mg^{2+} as green spheres. Generation of average structures is described in "Methods"; plots are generated with Normal Mode Wizard (https://academic.oup.com/bioinformatics/article/27/11/1575/217006).

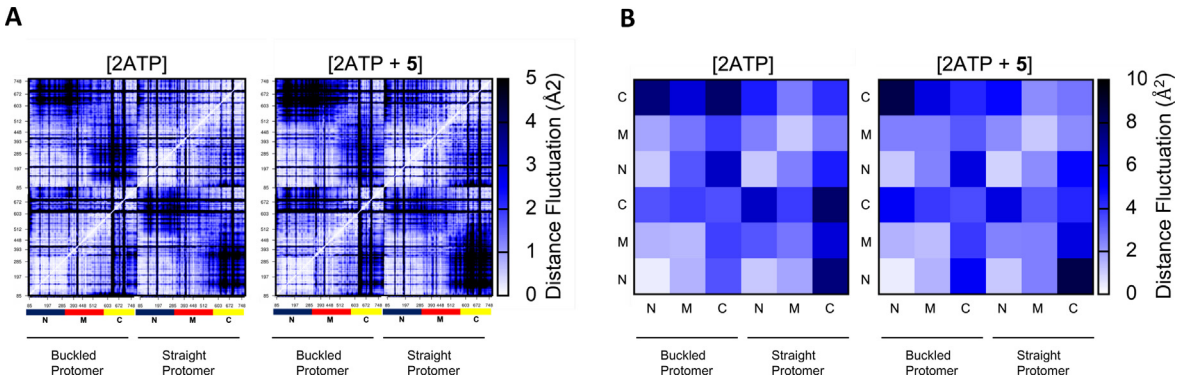

Figure 3. Distance fluctuation matrices for TRAP1 protomers in different ligand states, without and with bound compound **5**. **A.** Single residue representation: the magnitude of pairwise distance fluctuations is color coded from white (small fluctuations) to black (large fluctuations). **B.** Representation of distance fluctuations in terms of blocks corresponding to structural domains: N-terminal domain (NTD) from residue 101 to 308, Middle domain 311–571, C-terminal domain (CTD) residues 587–719 of both monomers.

domains and protomers alike is differentially modulated by the presence/absence of ligand **5**.

First, we calculated the distance fluctuations at the domain level: this calculation is carried out by subdividing the original residue-based matrix in blocks corresponding to the various domains and reporting only the average fluctuation of residues belonging to a certain domain with respect to the others. This block-representation of fluctuations shows that, in the presence of **5,** the NTD of the buckled protomer is less coordinated to the Middle and C-terminal domains of the other protomer compared to the [2 ATP] case. Furthermore, the fluctuations of the buckled protomer NTD with respect to the Middle and C-terminal domains of the same protomer are also slightly increased in the presence of **5**. The NTD of the straight protomer, in contrast, decreases its distance fluctuations (and thus increases its coordination) with the Middle and C-terminal domains of the other protomer (*cf.* lighter squares on the left). Interestingly, while **5** targets a binding pocket in the Middle domain of the straight protomer, its effects on the internal dynamics of the protein appear to diffuse to other regions of the protein important for function (Figure 3(b)): the correct positioning of the Middle domain with respect to the NTD is in fact strictly required to warrant the correct stereoelectronic organization of the active site to perform ATP hydrolysis. Interestingly, **5** perturbs this fine balance particularly in TRAP1 buckled protomer, which is the one where the first ATP hydrolysis takes place in the absence of allosteric ligands.

Next, to expose the aminoacids whose coordination patterns are most responsive (in a quantitative and statistically significant way) to the presence of **5**, we used a statistical approach based on F-tests, which we recently implemented.[62] In summary, the two distance fluctuation matrices appearing on the left-hand side of Figure 3 report variances in residue-pair distances, which are a measure of the dispersion of data points around a mean value. F-statistic is the ratio of these two variances, i.e. fluctuations in [2 ATP] *versus* [2 ATP + **5**]. The F-ratio is the ratio between two mean sum of squares (i.e. the sum of square deviations of a set of samples with respect to their average or with respect to a predicted value, divided by the number of degrees of freedom, *v*). The F-distribution is the cumulative distribution function of the F-ratio $F_{v1,v2}$ for the case that both sets of samples come from distributions with the same variance. Usually, the ratio is taken as the largest value, divided by the smallest value. If $F_{v1,v2}$ exceeds the 99% level, the probability that both sets of samples come from the same distribution is less than 1 percent. In the present case, the reference distribution is that generated by the [2 ATP] metatrajectory. If a fluctuation value in the [2 ATP + **5**] metatrajectory for a residue pair is significantly different according to F-statistic from the fluctuation value of the same residue pair in the [2 ATP] system, we give a score (F-score) of 1 to the difference. In case the difference is not significant, we give that difference a value of 0. For each residue *i*, this procedure is repeated for all pairs *i,j* where *j* are all the other residues in the sequence. Next, all scores for a certain residue (*i*) are summed up. The maximum value obtainable for the sum of each residue is N, where N is the total number of residues in the protein (here, the sum of the number of residues for each protomer). The results reported in Figure 4(a) show that a number of residues approaches the limit of N, which implies statistically significant differences between the matrix of pairwise distance fluctuation calculated for [2 ATP + **5**] *versus* [2 ATP].

To obtain a qualitative indication of the residues that change their dynamics upon binding of **5**, we processed the calculated F-scores to isolate those with significantly high values: we first calculated the mean and the standard deviation for the F-

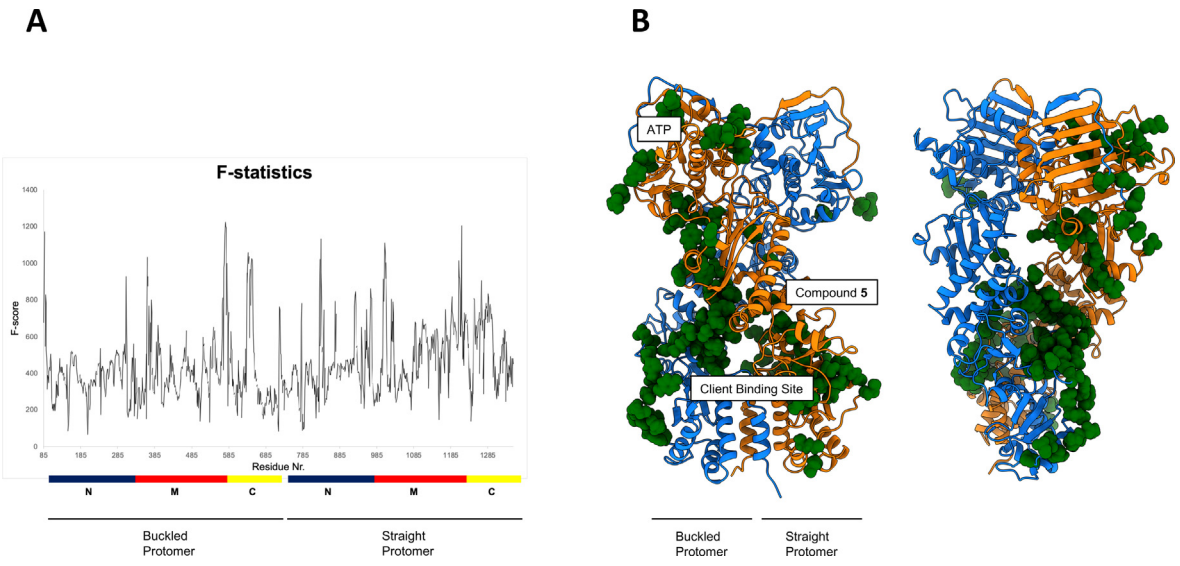

Figure 4. Identification of residues that modify their dynamics in response to compound 5 binding. **A.** The F-Score calculated for each residue of TRAP1 (ATP only state is the reference) reports on the statistical significance of the difference in fluctuations for each residue from the two DF matrices from figure 3a. The F-score is calculated according to the methodology described in the paper. **B.** Structural representation of the residues displaying the most significant differences in dynamics when compound **5** is bound with respect to the [2 ATP] case: residues that modify their dynamics are depicted as dark-green CPK models. Two orientations for TRAP1 are shown.

scores (Figure 4(a)) and filtered out the residues with an F-score smaller than the average plus one standard deviation. The remaining residues, deemed as the ones with the most significantly different dynamic profile, are projected on the structure in Figure 4(b). While this indication is qualitative, interestingly, identified residues are located, besides the vicinity of **5**, mainly around the ATP binding site (Figure 4(b)) and at the interface between the Middle and C-terminal domains. Interestingly, this region largely overlaps with the client binding site. Remodeling of the structures and dynamics of this interaction region may have a profound impact on TRAP1 protein–protein interactions: indeed, in our previous paper, we demonstrated that treatment with **5** inhibits TRAP1 interaction with its client protein Succinate Dehydrogenase (SDH).[36]

In summary, evident shifts in dynamics are observed when introducing **5**. They range from the perturbation of the local dynamics of residues important for regulating ATP processing and reactivity (as we also explain in the next subsection) and residues important for client recognition, to the relative fluctuations of domains in the closed state, up to modulation (of the initial stages) of the slow motions that may be associated with the large scale rearrangements required to TRAP1 to progress through the chaperone cycle. Overall, our results are an important indication that **5** can indeed to interfere with allosteric communication pathways across different areas of TRAP1.

Characterizing the impact of the allosteric ligand on chaperone reactive configurations. To better understand how the presence of **5** in the straight protomer impacts ATPase at the molecular and atomic level, we first set out to use our previously established model for TRAP1's reactivity[63] to compare and contrast the series of MD simulations of [2 ATP] and [2 ATP + **5**] carried out in this work. More specifically, using the same criteria as in our previous work,[63] we systematically quantify, for each system (*cf.* Methods), the frequency with which catalytically competent 'reactive poses' of ATP arise in the active site of each protomer. One such reactive pose is depicted in Figure 5(a), whereby the nucleophilic water $\mathbf{Wat_{Nuc}}$ (**N**), on top of having its oxygen in line to attack ATP:Pγ and being in a favorable orientation for deprotonation by Glu130:Oε, is only loosely sequestered by Tyr121 and its associated $\mathbf{Wat_{Tyr}}$ (**Y**), 2.50 Å away.

Our simulations point to an (expected),[63,64] general predominance of unreactive poses in both protomers (on average 17.2% and in general never exceeding 26% in either protomer in any individual replica; Figure S1) and in all cases, in line with experiment[29] and previous simulations,[63] the buckled protomer remains more reactive than the straight one in all cases, with more catalytically competent poses systematically found in the former (Figure S2). Nonetheless, bearing in mind these overarching conditions, some interesting patterns do emerge from our data when assessing possible effects of compound **5** on TRAP1's reactivity. We

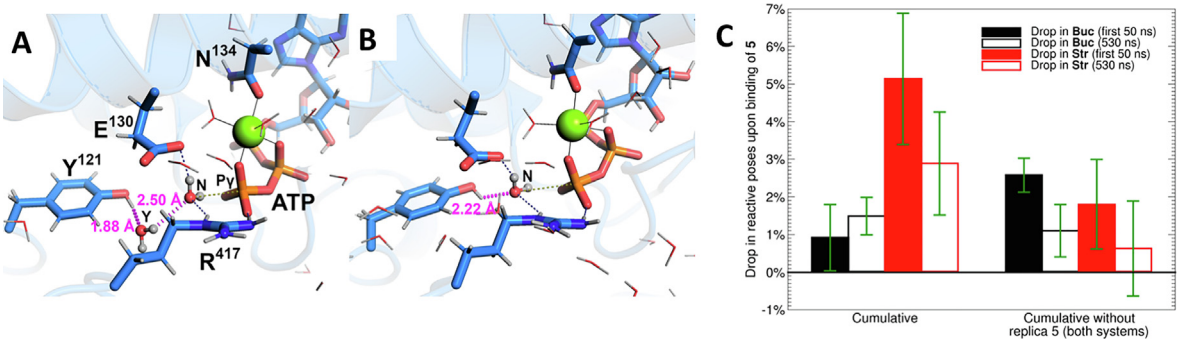

Figure 5. Organization of the Catalytic Site of TRAP1 and the Influence of compound **5**. **A.** Catalytically competent 'reactive pose' as defined by our previous reactivity model for TRAP1: the nucleophilic water $\mathbf{Wat_{Nuc}}$ (denoted by **N**) is in line to attack ATP:Pγ; prone to deprotonation by the general base Glu130; and only loosely sequestered by a $\mathbf{Wat_{Tyr}}$ (**Y**) that is interposed between it and Tyr121. **B.** Distinctive catalytically incompetent configuration prevalently occurring in the straight protomer during [2 ATP + **5**] MD run number 5 (and still only predominantly observed in that protomer and only in other [2 ATP + **5**] MD runs): here, $\mathbf{Wat_{Tyr}}$ is absent, and $\mathbf{Wat_{Nuc}}$ is directly hydrogen-bonded to Tyr121, hindering nucleophilic attack. Both scenes are rendered from similar perspectives, focusing on the active site of the straight protomer of zebrafish TRAP1 (**A.** is taken from a [2 ATP] run; **B.** from a [2 ATP + **5**] run). Key: catalytically relevant residue sidechains, ATP, and the Mg^{2+}-coordinating Asn134 are rendered as sticks and labeled in **A.**; salient $\mathbf{Wat_{Nuc}}$ and $\mathbf{Wat_{Tyr}}$ are rendered as ball-and-stick; other waters as lines; Mg^{2+} as a sphere; the rest of the protein is rendered as cartoon; Na^{+} ions are omitted for clarity. O: red; C: lighter blue; P: orange; N: darker blue; H: off-white; Mg: green. Hydrogen bonds relevant for $\mathbf{Wat_{Nuc}}$ sequestration/release by Tyr121 are shown in magenta; other catalytically relevant hydrogen bonds as dark blue dotted lines; the line of nucleophilic attack in dark yellow dotted. Solid black lines denote Mg^{2+}'s coordination sphere. **C.** Drop in reactivity observed in the presence of **5**, in the buckled protomer (**Buc**; black) and in the straight protomer (**Str**; red) assessed both throughout all MD simulations (empty bars), and throughout the first 50 ns of each replica only (filled bars). On the right, for the reasons explained in the main text, statistics are recalculated excluding replica 5 for [2 ATP] and replica 5 for [2 ATP + **5**]. Errors are calculated using the leave-one-out procedure.

present these over the next few paragraphs and elaborate on their general significance later on in the paper.

Changes in protomers' reactivity upon introducing **5** are plotted on the left-hand side of Figure 5(c): they are assessed across all 5 MD replicas of [2 ATP] *versus* all 5 MD replicas of [2 ATP + **5**], both over replicas' initial 50 ns—which should suffice to monitor reactivity[63,64]—as well as over their entire duration (530 ns), as a control. In this situation, and particularly over the first 50 ns (left-hand side, filled bars), we see that once **5** binds to the straight protomer, reactivity (*i.e.*, frequency of reactive poses) drops in both protomers: notably, however, this drop is significantly more prominent in the straight protomer than in the buckled (red *versus* black filled bars on the left). If replicas are considered in their entirety, differences between protomers mitigate, but a generalized drop in reactivity remains in both (left-hand side; black and red empty bars, respectively).

Our MD simulations point to the non-uniform emergence (*vide infra*) of a distinctive active site configuration (Figure 5**(b)**) in which the interposed water between Tyr121 and $\mathbf{Wat_{Nuc}}$ is displaced, leaving $\mathbf{Wat_{Nuc}}$ (**N**) directly hydrogen-bonded to Tyr121 (*cf.* 2.22 Å bond in Figure 5(b)). Were a hydrogen bond of this length to be found between $\mathbf{Wat_{Nuc}}$ and an interposed $\mathbf{Wat_{Tyr}}$, our criteria would identify the pose as 'reactive'; however, since chemical intuition suggests that a direct hydrogen bond between Tyr121:Hη and $\mathbf{Wat_{Nuc}}$:O should sequester the latter more strongly, we defined all such poses as catalytically incompetent. On the one hand, these peculiar poses were fleetingly observed in our previous work[63] and remain so in the present work insofar as both [2 ATP] protomers and [2 ATP + **5**]'s buckled protomer are concerned (with frequencies never exceeding 1%; Table S1). On the other hand, in replicas 3 and 5 of [2 ATP + **5**] direct sequestration of $\mathbf{Wat_{Nuc}}$ by Tyr121 in the (**5**-bound) straight protomer is much more frequent, at 6.55% and 70.37% of the total poses, respectively (Figure 5 **(c)**).

The conspicuously unequal distribution of this distinctive 'unreactive pose', in which the nucleophile is directly sequestered by Tyr121, has inevitable repercussions on the general reactivity statistics (perhaps best recognizable in Figure S1). Ultimately, given this significant imbalance, we cannot confidently establish to what extent the predominance of this situation in [2 ATP + **5**]'s MD replica 5 is indeed a rare event, as this would require more replicas and is beyond the scope of this work: for this reason, on the right-hand side of Figure 5(c) we have chosen to present a revisited set of statistics in which [2

ATP + **5**]'s MD replica 5 is excluded and, to make the comparison fair, the same is arbitrarily done with [2 ATP]'s replica 5. This revisited set of statistics confirms a general drop in reactivity in both protomers upon binding of **5**.

In general, despite complex trends that reflect the complexity of the hydrolysis mechanism involved, results from these analyses help define a mechanistic model consistent with the experimentally observed inhibition of TRAP1 ATPase induced by compound **5**.

Finally, further to the role of asymmetry and **5** in shaping protomers' reactivity, it is interesting to note that differences in water distribution in the two protomers' active sites emerge most prominently when viewed with respect to Tyr121 and with respect to ATP, even when [2 ATP + **5**]'s atypical configuration from its replica number 5 is taken into account (Figure 5**(b)**). Indeed, radial distribution functions of water around key catalytic residues and ATP:Pγ over the first 50 ns of [2 ATP] and [2 ATP + **5**] replicas (Figure S3) clearly show the greatest differences between protomers (and, though less so, when **5** is present or absent) when measured around Tyr121:Hη and ATP:Pγ for the $\mathbf{Wat_{Nuc}}$ and $\mathbf{Wat_{Tyr}}$ peaks. On the other hand, virtually no differences are observed in the distribution of $\mathbf{Wat_{Nuc}}$ around the catalytically crucial general base (Glu130); and only a slightly greater accumulation of $\mathbf{Wat_{Nuc}}$ in the buckled protomer around the stabilizing Arg417 finger (also observed in our previous work).[63] These observations suggest that **5** too, like protomer asymmetry, should principally alter reactivity by 'acting' allosterically on Tyr121 and $\mathbf{Wat_{Tyr}}$.

Design of second generation allosteric ligands. The results reported in the previous paragraphs support a model in which small molecule **5** allosterically perturbs the functionally-oriented dynamics of TRAP1 at different levels. Computational data are consistent with the experimentally observed inhibitory effects of **5.**

We next asked ourselves whether we could exploit dynamics-based data on the crosstalk between **5** and TRAP1 to discover ligands with better activities. Our reasoning is the fact that protein dynamics and flexibility determine ligand poses and, additionally, ligand poses influence pocket conformations.[31,46,65,66] This represents the structural basis for further ligand development. To start exploring the validity of this hypothesis, we characterized the potentially druggable pockets formed during MD around ligand **5** in the most representative structures obtained from clustering analysis of the [2 ATP + **5**] metatrajectory (see *Methods*). To this end we used the SiteMap tool of the Maestro Software.[67] SiteMap returns a visual representation of the physicochemical properties of the binding site, combined to a druggability score. In general, binding sites are pictorially characterized by: i) white balls to indicate the available volume; ii) yellow clouds to outline hydrophobic regions; iii) blue and red clouds to highlight H-bond donor and H-bond acceptor, respectively. We applied this type of analysis in the region comprising compound **5** and around it.

In Figure 6**(a)**, we report the structure of TRAP1 bound to **5**, with a zoom into the 3 main conformations of the pocket around 5 explored during the simulation. Interestingly, all pockets share one common trait, i.e. a wide hydrophobic region (occupied almost entirely by **5**). Cluster analysis of the metatrajectory shows that **5** forms π-interactions (see Figure 6(b) for an example with Arg895 or Arg957). Furthermore, the data show different available volumes not occupied by the ligand, and an unexploited region where forming H-bonds may prove beneficial to ligand binding. To design new derivatives, we used as structural targets the 3 representatives of the most populated structural clusters emerging from the cluster analyses described in Methods. Furthermore, we analyzed the pocket in conformations extracted every 100 ns from the metatrajectory.

On this basis, we used the Ligand Designer and Interactive Pose Prediction tools from the Maestro Software Suite to design modifications on the initial lead. The lead was modified looking for additional/better interactions within the different conformations of the pocket. This design stage was in fact carried out with the goal of designing compounds that would maintain the main interactions (π-cation interaction with Arg residues or π-π interactions with aromatic side-chains) displayed by **5**, while improving the ligand–protein interaction score (through the possible exploitation of additional stabilizing interactions such as H-bonds) (Figure 7). The interaction score is calculated simply as a Glide score, which is a drug-optimized docking energy function implemented in Maestro (www.schrodinger.com, Table S2). The minimum energy value observed for each design in any conformation of the pockets described above (and in Methods) was annotated and used to guide subsequent synthetic efforts. No additional docking of the designs was used at this stage.

The designed compounds **51**–**57** are reported in Figure 1(b). This series was next synthesized and characterized (see Supplementary Material) and experimentally probed in biochemical and cell tests.

Experimental validation of the designs in biochemical and cell experiments

Compound 5 derivatives inhibit TRAP1 ATPase cycle. We used an ATP-regenerating system[68] to determine whether the seven compound **5** derivatives (**51**–**57**) could act as TRAP1 inhibitors. It has to be noted that compounds **54** and **56** are biotinylated derivatives which will be

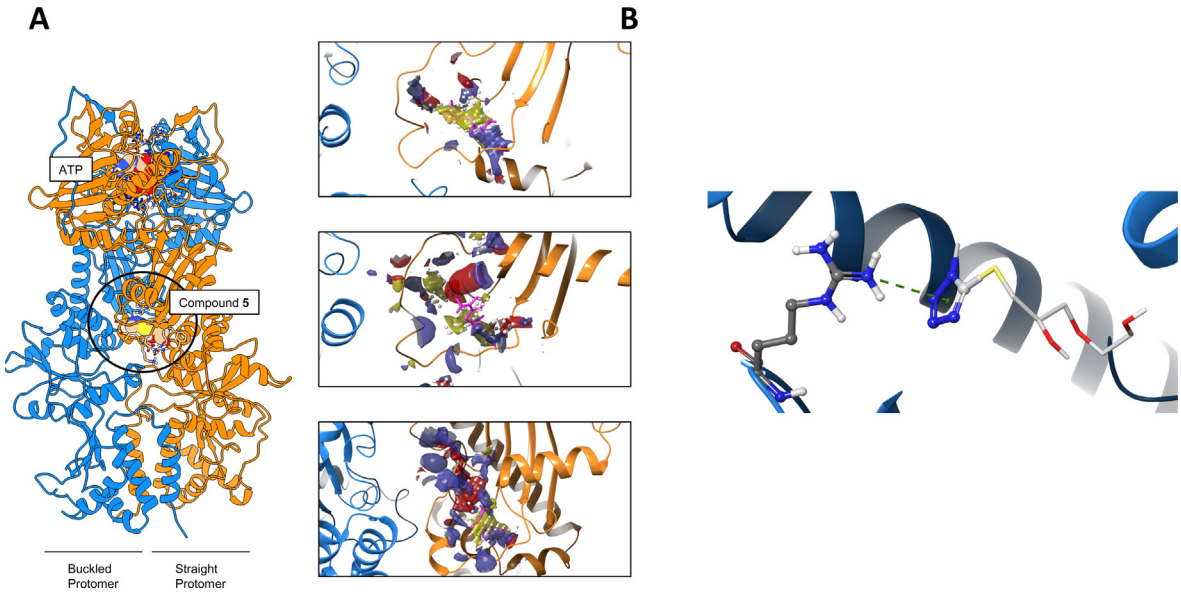

Figure 6. TRAP1 bound to compound **5** and the formation of pockets around it. **A.** The complex TRAP1-compound **5** (colored according to atom type) and the zoom in on three representative pockets around compound **5** from three different clustering methods described in the Methods section. **B.** A representative π-cation interaction, green dotted line, between tetrazole of compound 5 and Arg895, in this case, of TRAP1.

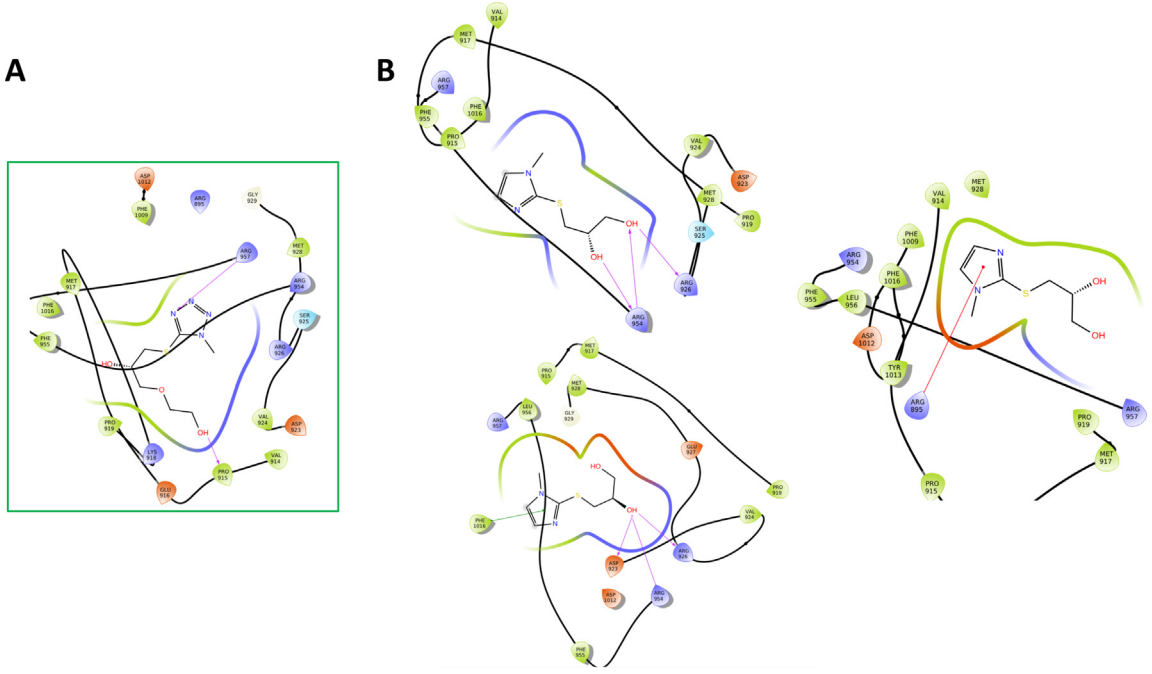

Figure 7. Ligand Interactions and Design. **A.** A schematic representation of the main interactions made by compound **5** used to drive the design of second-generation ligands. **B.** The ligand interaction map of newly designed compound **51** in different representative conformations of the protein, visited during the dynamics in the presence of compound **5.**

used in the future for pull-down experiments. Here, we aim to test only that the introduction of the appendage does not influence biochemical and cellular activities. We found that all molecules were able to inhibit TRAP1 ATPase activity (Figure 8), with some of them displaying a degree of inhibition similar to that of the lead compound **5.**[36] Compounds **51**, **52**, **56** and **57** were highly selective TRAP1 inhibitors, as they could not inhibit Hsp90 ATPase activity (Figure 8(a)). Then, we chose the

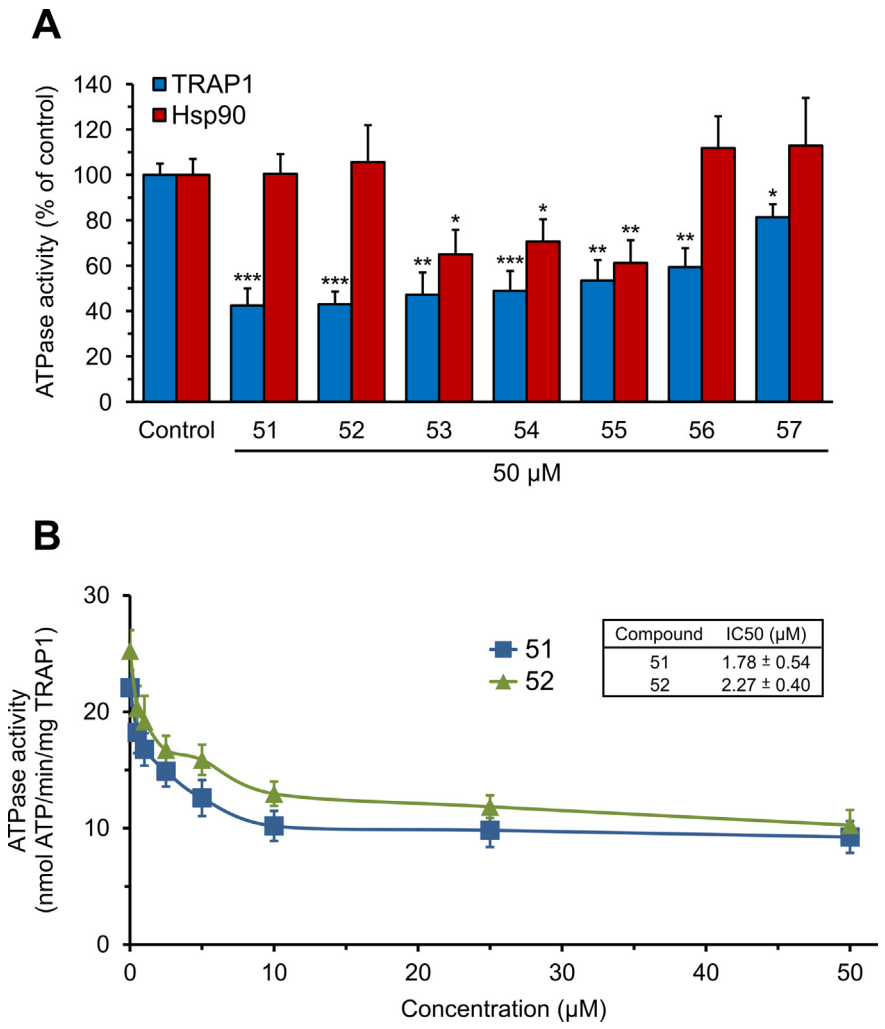

Figure 8. Effects of a set of compound **5** derivatives on TRAP1 and Hsp90 ATPase activities. **A.** Spectrophotometric quantification of the effects of second-generation TRAP1 inhibitors (50 μM each) on the ATPase activity of purified human TRAP1 and Hsp90α proteins (blue and red bars, respectively). Mean ± standard error of the mean (SEM) data (n = 3 independent experiments) are shown as normalized values with respect to vehicle-treated protein samples. ***$p < 0.001$; **$p < 0.01$; *$p < 0.05$ with an unpaired two-tailed Student's *t* test. **B.** Dose-response analysis of the effects of compounds **51** and **52** (blue and green traces, respectively) on the ATPase activity of human recombinant TRAP1. Data are shown as mean ± SEM (n = 3 independent experiments).

most active and selective molecules, **51** and **52**, for further characterization. A dose–response analysis showed that both compounds induced a concentration-dependent inhibition of TRAP1 ATPase activity (Figure 8(b)) with half-maximal inhibitory concentrations (IC50) in the range of 2 μM, lower than those estimated for first-generation TRAP1 ligands, which were around 10 μM.

Second-generation molecules revert TRAP1-dependent SDH inhibition. We have previously reported that TRAP1 downregulates the enzymatic activity of SDH in various tumor cell types,[33,36,53,69–72] and that this inhibition can be overturned by allosteric TRAP1 inhibition.[33,36,72] We have also shown that SDH inhibition is favored by ERK-dependent TRAP1 phosphorylation in tumor cells endowed with hyperactivation of the Ras/ERK signaling pathway, such as cellular models of malignant peripheral nerve sheath tumors (MPNST), where TRAP1 has been identified as an important determinant of their pro-neoplastic features.[52] Therefore, we measured the succinate-coenzyme Q reductase (SQR) activity of SDH as a read out to determine the efficacy of the selected second-generation inhibitors in cells. As expected, knocking-out TRAP1 expression by CRISPR/Cas9 technology enhanced the SQR activity of SDH in a mouse MPNST cell model, sMPNST cells (Figure 9(a)). Treatment with compounds **51** and **52** increased enzymatic SDH activity to the same extent reached by TRAP1 knockout cells, which were completely insensitive to the compounds (Figure 9(a)). Notably, compound **51** was able to revert SDH inhibition faster than compound **52**. This

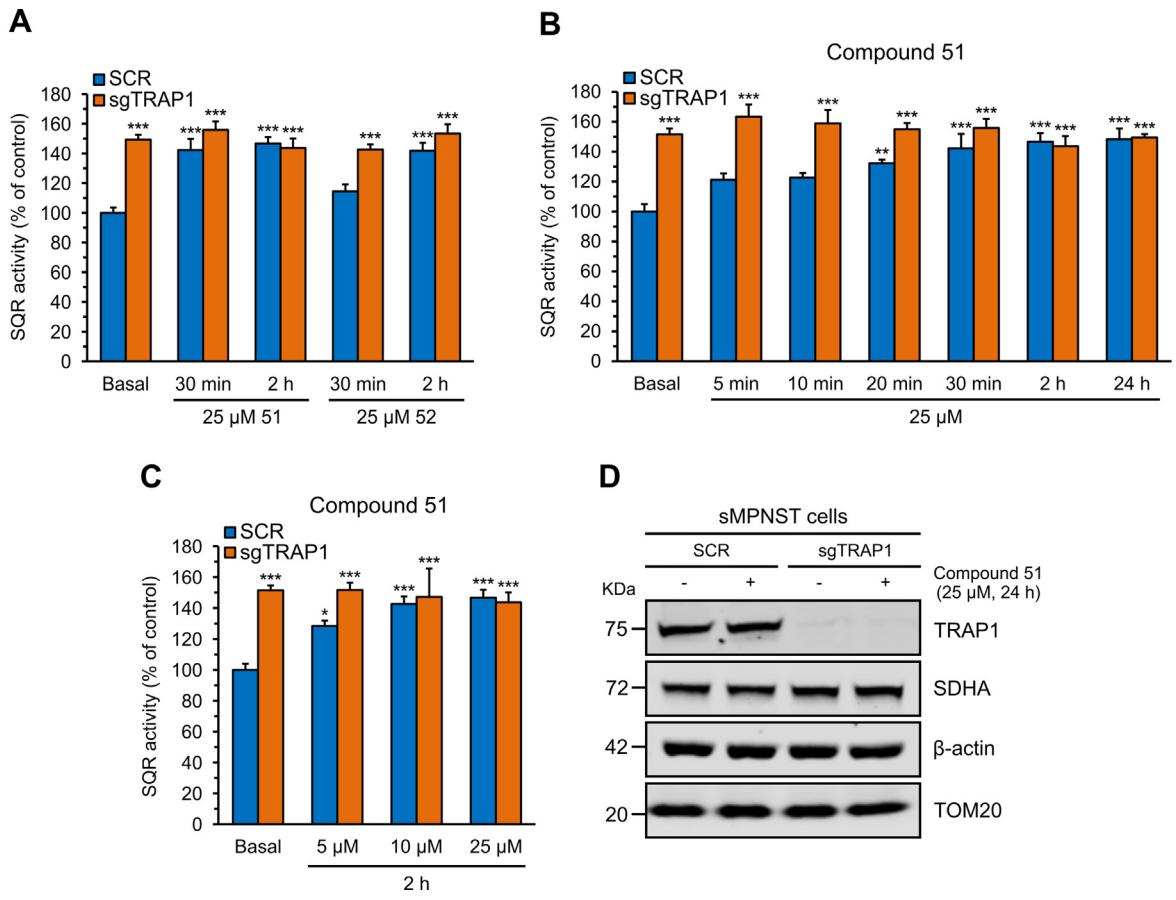

Figure 9. Allosteric TRAP1 inhibition induced by compounds **51** and **52** increases SDH enzymatic activity. **A.** Spectrophotometric assessment of the succinate:coenzyme Q reductase (SQR) activity of SDH on TRAP1-expressing (scrambled, SCR) and TRAP1 knockout (sgTRAP1) sMPNST cells treated with compounds **51** and **52** (25 μM each) for the indicated times. **B.** Kinetic analysis of the effect of compound **51** on SQR activity. **C.** Dose-response analysis of a 2-h cell exposure to the reported concentrations of compound **51**. Data are reported as mean ± SEM (n = 3 independent experiments). ***$p < 0.001$; **$p < 0.01$; *$p < 0.05$ with one-way ANOVA with post-hoc Bonferroni's test against SQR activity values in vehicle-treated scrambled cells. **D.** TRAP1 and SDHA expression levels in sMPNST cells treated with compound **51** for 24 h. Beta-actin and TOM20 were used as cytosol and mitochondria loading controls, respectively. TRAP1 expression was previously knocked-out using the CRISPR/Cas9 technology.

effect of compound **51** was stable over time (Figure 9(b)), occurred in a concentration-dependent way (Figure 9(c)) and did not change either TRAP1 or SDHA protein expression levels (Figure 9(d)).

Compound 51 abolishes tumorigenic features of TRAP1-expressing neoplastic cells. We have previously demonstrated that TRAP1-mediated inhibition of SDH activity is increased when neoplastic cells are placed under stress conditions that mimic those found during tumor progression,[69] and that TRAP1 activity is required for *in vitro* tumorigenic growth of various tumor cell models.[52,69] Thus, we assessed whether allosteric inhibition of TRAP1 induced by compound **51** might alter tumorigenic properties of sMPNST cells, evaluated by a focus forming assay. As expected, TRAP1-expressing tumor cells overcame contact inhibition and formed foci. Treatment with compound **51** dramatically reduced foci formation, phenocopying the effect of knocking out TRAP1 expression (Figure 10).

Discussion

The design of isoform selective ligands is an active subject of research, with important implications in chemical biology, medicinal chemistry, and biomedicine. While previous research work focused on the design of Grp94[31] and Hsp90α/β[32,66,73–76] specific inhibitors, scarcer information is available on TRAP1 selective inhibitors.[77,78] We were among the first ones to devise a successful strategy for selective TRAP1 targeting.[36]

The difficulty in characterizing allosteric ligand effects is that the Structure-Activity-Relationships (SARs) of these compounds are often very

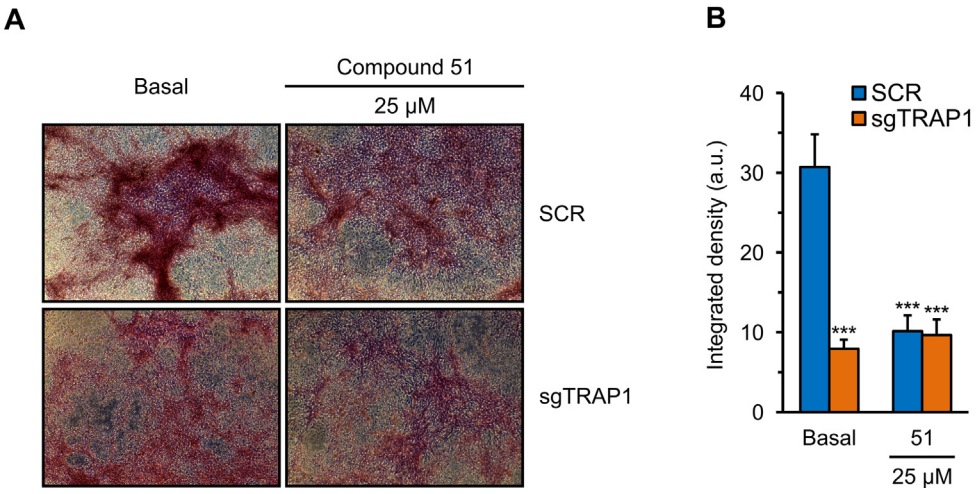

Figure 10. Effects of compound **51** on *in vitro* tumorigenesis. **A.** Representative pictures of foci formed by TRAP1-expressing (scrambled, SCR) and TRAP1 knockout (sgTRAP1) sMPNST cells treated with compound **51** for 9 days. **B.** Quantification of the effect of TRAP1 inhibition, either by treatment with compound **51** or by its genetic ablation, on focus growth. Data are presented as mean ± SEM (n = 3 independent experiments). ***p < 0.001 with one-way ANOVA with post-hoc Bonferroni's test against integrated density values in vehicle-treated scrambled cells.

complex. Allosteric ligands are in fact intended to bind to a dynamic site that does not overlap with, and is far removed from, the active site where the actual enzymatic function takes place. In many cases, no direct correlations between the binding affinity values (calculated or experimental) and effects on protein (chaperone) functions or cellular activities could be observed. These considerations are general and reflect the unique challenges posed by allosteric modulators to drug-design as well as the need to develop innovative models to predict ligand activities.[43,79,80] Indeed, experimental tests generally measure orthosteric function and not what actually happens in terms of binding affinity and kinetics at the allosteric site. In this context, the Gestwicki lab reported for instance that allosteric inhibitors of Hsp70 with a somewhat low affinity for the protein in vitro could still show relevant activity in client refolding tests and cell-based aggregation assays.[81] In contrast, compounds with a superior affinity for Hsp70 featured reduced activities in cells when compared to the parent lead.

Optimizing allosteric modes of action requires methods that may substantially different from those used in orthosteric drug discovery, where improving affinity for a binding site is the major objective.

These considerations underline the need for simple and general methods that allow to identify functionally relevant allosteric sites and help evolve molecular entities that engage the target, determining an efficient modulation of its activity. To answer this question, in this work we have presented a general strategy that reconnects basic studies of allostery in large proteins, through atomistic simulations, with the discovery of ligands with interesting biochemical and cellular activities.

Here, we started from the detailed computational characterization of the impact of a recently designed active TRAP1 allosteric inhibitor on the functionally-oriented aspects of the chaperone's structural dynamics. The results and trends observed, though mostly qualitative, are in general agreement with experimental observations, and provide a detailed mechanistic understanding of the effects of allosteric ligand binding. Combining the considerations emerging from the analysis of large scale dynamics, internal coordination patterns, and organization of the active site upon introduction of **5**, three mutually exclusive scenarios can be formulated: (1) that **5** widens the gap in reactivity between the buckled and straight protomer even further—making the latter comparably even less reactive than observed[29] in [2 ATP]; (2) that **5** induces a generalized drop in reactivity in both protomers—such that ATPase rates drop overall but the buckled protomer remains more reactive by a similar amount; or (3) that, as observed without replicas number 5 of [2 ATP] and [2 ATP + **5**] over longer timescales (Figure 5, right-hand side; empty bars), **5** mainly quenches reactivity in the buckled protomer from its allosteric site on the straight protomer, influencing its dynamics and coordination relative to the Middle and C-terminal domains. Though none of these scenarios may be categorically ruled out by our simulations, in any one of them the presence of **5** clearly reshapes the structural dynamics of the client binding region, thus affecting recognition of client proteins, as proved by Sanchez-Martin *et al.*[36]

More specifically, the presence of **5** results in a clear perturbation of the functional motions of the closed, active state of the protein, which translate to a drop in reactivity in at least one of the two

protomers. In other words, **5** has the potential of perturbing TRAP1's conformational cycle in at least one of its stages: this is a very significant finding that further validates our *in silico* model, and is entirely in line with our biological data, which pinpoints **5** as an inhibitor of TRAP1 biochemical and cellular activities.

With regards to the theme of structural asymmetry, though this aspect was not central to the present study, we should also stress that our simulations once again correctly capture the buckled protomer's greater reactivity compared to the straight one, regardless of the presence of **5** in the latter, *i.e.*, in [2 ATP] and [2 ATP + **5**] alike. Besides being in line with experimental data for [2 ATP],[29] this suggests that **5**'s allosteric effects on reactivity should be more subtle and/or articulated compared to those brought about by sheer protomer asymmetry.

One important advancement of our study is represented by the possibility to design second-generation derivatives based on the characterization of the dynamic crosstalk between the protein and a first generation ligand. Here, we propose a simple and straightforward approach that proves to deliver a compound with a better drug-like profile and improved biochemical and cellular activities. In this context, perturbation of TRAP1 enzymatic reactivity and dynamics reverberates in the modulation of the chaperone's client interaction profiles, in particular with client SDH. Since the designed compounds are selective for TRAP1 (and do not have significant activity on the paralog Hsp90), these new molecules may represent fundamental starting points for the development of inhibitors TRAP1-centered pathways. Considering the importance of TRAP1 in different types of diseases, these new molecules have the potential to be developed into inhibitors with unique therapeutic potential.

While based on the particular case of TRAP1, this methodology is completely general and can be extended to other targets where allosteric modulation represents an interesting therapeutic option.

Methods

Computational approaches

System preparation. The reference TRAP1 structure for all simulations is crystal structure 4IPE.pdb,[82] with missing fragments modeled based on previous simulations[36,56]; both protomers were thus reconstructed without gaps from Thr85 to His719.

To reconstruct ATP, the Nβ atom of the adenylyl-imidodiphosphate molecule that is present in each protomer's active site is replaced by oxygen, and its bound hydrogen atom deleted; all cations are also removed, except for the Mg^{2+} present in each active site. *N*- and *C*-termini are capped with acetyl and *N*-methyl moieties, respectively: in the latter case, this is to avoid open $-NH_3^+$ caps disrupting a functionally crucial inter-protomer interaction between His87 and Glu157.[82]

All hydrogens are added (or replaced *post*-docking) using *AmberTools*' *tleap* utility (version 19),[83] with residues calculated to be in their standard protonation states at physiological pH. Both protomers' histidines 103, 144, 525, 553, and 719, as well as (buckled) protomer A's histidines 573 and 635, are modeled with Nδ protonation; conversely, Nε protonation is introduced on the remaining 20 histidines.

Retaining 18 crystallographic water molecules in each protomer's active site, *tleap* is also employed to solvate our structures in an isometric truncated octahedral box of water, ensuring a distance of at least 10 Å between every protein atom and the closest edge.

Docking

Briefly, compound **5** is docked into the allosteric binding site as already described in.[36] The GLIDE docking program (Glide, version 6.9, Schrödinger, LLC, New York, NY, 2015) was used to target the binding site defined in.[36] Rigid receptor and flexible ligand docking calculations were performed in standard precision mode (SP) with the OPLS_2005 force field, nonplanar conformations of amide bonds were penalized, van der Waals radii were scaled by 0.80, and the partial charge cutoff was fixed to 0.15. No further modifications were applied to the default settings. The best docking pose according to the docking score function was selected as a starting point for further MD simulations.

Forcefield parameters for molecular dynamics simulations and parametrization of 5

During Molecular Dynamics simulations (MD), protein residues are modeled using *ff14SB* forcefield parameters.[84] Parameters adopted for ATP are those published by Meagher and coworkers,[85] whereas those for Mg^{2+} are the ones reported by Allnér *et al.*[86] The chosen water model is TIP3P[87] which is compatible with parameters by Joung and Cheatham[88] chosen to treat Na^+ cations.

Compound 5 parametrization is carried out with the aid of *AmberTools*' *antechamber* and *parmchk2* utilities.[83] *GAFF* parameters[89] are introduced to model Lennard-Jones interactions and bonded interactions (dihedrals, angles, bonds). Derivation of point charges is carried out using the *Gaussian09* program[90] in conjunction with *antechamber*: first, compound **5** is structurally optimized at the B3LYP/6-31G(*d*) level of density functional theory (DFT); subsequently, ESP charges[91] around each atom are calculated based

on the electrostatic potential, calculated at the Hartree-Fock/6-31G(*d*) level, and sampled over 10 shells per atom at a density of 17 grid points per square Bohr; final atomic point charges are assigned after RESP fitting[92] performed by *antechamber*.

Molecular dynamics simulations

MD simulations are carried out using the *Amber* suite (version 18)[93] with the *sander* MD engine employed in the early preproduction stages (minimization) of each MD run, and the GPU-accelerated *pmemd.cuda* utility[94] thereafter. Five independent MD replicas (atomic velocities assigned from different random seeds) are carried out for each system, comprising minimization, preproduction, and production (*vide infra*): after minimization, temperature control is enforced throughout *via* the Langevin thermostat;[18] the integration timestep employed throughout is 2 fs; and bonds containing hydrogens are constrained using the *SHAKE* and *SETTLE* algorithms.[95]

Minimization in each replica consists of two (identical) rounds. The first (500 steepest descent + 500 conjugate gradient steps) excludes Mg^{2+}, and all protein and ATP heavy atoms (plus those of the ligand, if present): these are positionally restrained by a 500 kcal mol^{-1} $Å^{-2}$ harmonic constant. The second round (1000 + 1500 steps) involves the entire system. Minimization is followed by assignment of atomic velocities, and a rapid heating step from 0 to 300 K (20 ps; *NVT* ensemble) in which positions of protein, ATP, and ligand heavy atoms when present are gently restrained with a 5 kcal mol^{-1} $Å^{-2}$ constant. At this stage, coupling to the thermostat is weak (0.75 ps^{-1} collision frequency), and the cut-off for the calculation of Lennard-Jones and Coulomb interactions is 10 Å, beyond which only the latter are computed, but switching to the particle mesh Ewald method.[96] There follows an equilibration step (4 ns; *NpT*), wherein restraints are released, coupling to the thermostat is tightened at 2 ps^{-1}, and a constant pressure of 1 bar is introduced *via* Berendsen's barostat (2 ps relaxation time).[97]

Production runs (530 ns; *NpT*) are run under the same conditions as the equilibration step, except that the cutoff to directly compute Lennard-Jones and Coulomb interactions is shortened to 8 Å.

Quantification of reactive poses

Quantification of 'reactive poses'—*i.e.*, MD snapshots in which the nucleophilic water **Wat_{Nuc}** is in a catalytically favorable position to kickstart ATP hydrolysis—and derivation of the associated radial distribution functions (RDFs) was performed using *AmberTools*' *cpptraj* utility[93] using the same criteria (*vide infra*) that some of us derived and adopted in a previous study.[63] All reactivity statistics are considered both individually, over each system's five independent replicas, and collectively, *i.e.*, with individual replicas concatenated into a single 2.65 μs metatrajectory.

We consider a pose 'prone to react' if: (1) **Wat_{Nuc}**:O is $\leq$ 3.40 Å away from ATP:Pγ and attacks 'in-line' (*i.e.*, the angle **Wat_{Nuc}**:O --- ATP:Oγ – ATP:Oβ is comprised between 150° and 180°); (2) one of **Wat_{Nuc}**:H is $\leq$ 2.25 Å away from the general base Glu130:Oε(1/2) (Glu115 in TRAP1); (3) **Wat_{Nuc}**:O is *more loosely* sequestered (hydrogen bond: $\geq$ 1.87 Å) by a second water interposed between Tyr121 (Tyr 106 in TRAP1); (4) Mg^{2+} retains sixfold coordination to ATP:O(α,β,γ), Asn134:Oδ1 (Asn119 in TRAP1); and 2 H_2O (all six $\leq$ 2.30 Å); and (5) both **Wat_{Nuc}** and one ATP:Oγ retain hydrogen bonds to Arg417 (Arg 402) (at $\leq$ 2.85 Å and $\leq$ 3.00 Å, respectively).

A peculiar situation predominantly arising in one MD replica of the Compound 5-bound system, whereby **Wat_{Nuc}** in the straight protomer is directly sequestered by Tyr121 (Tyr106) rather than by the interposed water, is considered to be 'unreactive'.

Errors in cumulative reactivity statistics are calculated using the "leave-one-out" approach, in which statistics for each system are systematically recalculated by excluding a different replica each time. The standard deviation of these recalculated values (one per protomer per system) represents the error. When assessing reactivity differences between two protomers *X* and *Y* (within the same system or with *versus* without compound **5**), the resulting error E_Δ is determined from the original errors E_X and E_Y as $(E_X^2 + E_Y^2)^{0.5}$.

Principal component analysis

PCA for both systems is entirely carried out using several functions in the *cpptraj* tool, only taking into account heavy protein atoms (henceforth "reference atoms")—*i.e.*, protein hydrogens, solvent molecules, ATP molecules, cations, and, if present, the ligand are all excluded.

First, each system's individual MD replicas are again concatenated into a 2.65 μs metatrajectory but, this time, structures are also aligned on reference atoms of the first frame in the first replica. From each aligned metatrajectory we eliminate everything but the reference atoms and derive an artificial average structure: this then serves as a reference for the calculation of the covariance matrix of our reference atoms throughout the metatrajectory itself. Eigendecomposition of each system's covariance matrix yields its principal components (as eigenvectors).

Distance fluctuation analysis

To understand the impact of the ligand on the internal dynamics of TRAP1 we conducted the distance fluctuation analysis.

We used the same 2.65 μs metatrajectory, obtained concatenated the MD replicas of both systems to compute the matrix of distance fluctuations in which each element of the matrix corresponds to the CP parameters:

$$DF_{ij} = \langle (d_{ij} - \langle d_{ij} \rangle)^2 \rangle$$

where d_{ij} is the time-dependent distance of the C α atoms of amino acids *i* and *j* and the brackets indicate the time-average over the trajectory. In this case the DF matrix has been used to assess not only the intrinsic flexibility of proteins but also to understand its changes upon ligand binding.

The DF was calculated for any pair of residues during the trajectory. This parameter characterizes residues that move in a highly coordinated fashion, and it is able to reflect the presence of specific coordination patterns and quasi-rigid domains motion in the protein of interest. In particular, pairs of amino acids belonging to the same quasi-rigid domain are associated with small distance fluctuations and vice versa.

Statistical quantification of differences among DF matrices

We implemented a statistical analysis based on F-tests (F-statistic) to quantitate the significance of the differences observed among DF matrices.

DF matrices substantially report the variances in the distances between every residue pair in the protein. In general, variances measure the dispersion of data points (different measures) around their respective means. An F-statistic is the ratio of two variances and an F-ratio is the ratio between two mean sum of squares (i.e. the sum of square deviations of a set of samples with respect to their average or with respect to a predicted value, divided by the number of degrees of freedom, v). The F-distribution is the cumulative distribution function of the F-ratio $F_{v1,\ v2}$ for the case that both sets of samples come from distributions with the same variance. It is usual to take the ratio as the largest value, divided by the smallest value. If $F_{v1,v2}$ exceeds the 99% level, the probability that both sets of samples come from the same distribution is less than 1 percent.

With this statistic, we compared the respective values of DF for all residue pairs across the various simulations. As a reference, in comparing different matrices, we selected the DF matrix of the double ATP state. If a DF value for a residue pair in a certain simulation is significantly different according to F-statistic from the DF value of the same residue pair in the reference system, we give a score of 1 to the difference. In case the difference is not significant, we give that difference a value of 0. Given a residue *i*, we repeat this procedure for all pairs *i,j* where *j* are all the other residues in the sequence. At the end, all scores for a certain residue are summed up. The maximum value obtainable for the sum of each residue is N, where N is the total number of residues in the sequence. Summing up all the scores for all residue pairs, one can obtain a maximum value of N^2.

Clustering

Four different clustering methods were implemented to analyze pocket formation.

After running the MD simulations, structural cluster analysis was run on each metatrajectory to obtain the most representative conformations of the systems under study.

For the analysis of TRAP1 bound to compound **5**, we used the hierarchical agglomeration algorithm described in[98] with the following parameters: we set an Epsilon of 10.0, while the maximum number of clusters obtainable by the algorithm was set to 6.

Three different metrics were used to define the differences between structures, all based on RMSD:

1. The first method includes all residues of the Straight protomer (containing compound **5**) and loops not organized in secondary structures of the Buckled protomer. RMSD was calculated on the backbone atoms.
2. In the second approach, an average structure based on the whole metatrajectory of the TRAP1-compound **5** complex was calculated, and the residues within 6 Å from compound **5** were retained for clustering. The clustering was run on heavy atoms of the side chain of selected amino acid residues.
3. In the third approach, the heavy atoms of compound **5** (C, S, O, N) were used as reference.

Additionally, a time-dependent "control" approach was used: we isolated the frames every 250 ns, and we replicated all the aforementioned analyses on these structures.

The results of each clustering analysis yielded approximately 80% representativity with the top 3 most populated clusters, on which we searched for druggable pockets around the location of **5**.

Pocket analysis

Analysis of pockets was carried out on the representative structures of the most populated clusters described above.

The search for possible pockets on MD-selected structured of the complexes was carried out with the use of Sitemap,[99] a tool of the Maestro Suite (www.schrodinger.com), specifically developed for the identification of drug/lead binding pockets on the surfaces of the proteins of interest. In this case, we searched the pockets around the region of

compound **5**. The tool allows to select a mask around which to search: we selected compound **5** as reference and researched all pockets within 10 Å. Using the default setting, we retain the five best pockets in this site.

Experimental Approaches

Compounds

Seven second generation TRAP1 inhibitors (compounds **51**–**57**) were used in *in vitro* and *in cellulo* assays. The synthesis and characterization of the compounds is described in the Supporting Information. These compounds were dissolved in dimethylsulfoxide (DMSO, Sigma-Aldrich) and added at the indicated concentrations. An equal quantity of DMSO (lower than 0.1%) was added to control samples.

Protein purification and production

Full-length recombinant human TRAP1 (without mitochondrial signal sequence) was cloned into the pET151/D-TOPO bacterial expression plasmid (Thermo Fisher Scientific) as a TEV-cleavable N-terminal His-tagged fusion protein.[29] TRAP1 expression was induced in BL21-AI *E. coli* cells (Thermo Fisher Scientific) grown in LB media (Sigma-Aldrich) by addition of 1 mM isopropyl 1-thio-β-D-galactopyranoside (Promega) and 0.2% arabinose (Sigma-Aldrich) at OD600 ≈ 0.7–0.8 and then incubated under shaking for 20 h at 16 °C. Purification followed a standard protocol for Ni-NTA chromatography using a buffer composed by 50 mM KH_2PO_4 (Merck), pH 8.0, 300 mM NaCl (Sigma-Aldrich), 500 mM imidazole (Sigma-Aldrich) and 3 mM β-mercaptoethanol (Sigma-Aldrich). Samples containing recombinant TRAP1 were then dialyzed overnight and stored at −80 °C.

TRAP1 and Hsp90 ATPase activity measurements

TRAP1 and Hsp90 activities were determined using the previously described ATP-regenerating system.[100] All experiments were performed in an assay buffer containing 50 mM Tris-HCl, pH 7.4 (Sigma-Aldrich), 50 mM Sucrose (Sigma-Aldrich), 50 mM potassium chloride (Sigma-Aldrich), 4 mM magnesium chloride (Sigma-Aldrich), 2 mM EGTA (Sigma-Aldrich), 300 μM NADH (Sigma-Aldrich), 2 mM phosphoenolpyruvate (Sigma-Aldrich), 1.5 mU/mL L-lactate dehydrogenase (Sigma-Aldrich), 0.8 mU/mL pyruvate kinase (Sigma-Aldrich) and 450 ng human recombinant TRAP1 or Hsp90α (Enzo Life Sciences). Kinetic assays were started after addition of ATP and activity was measured by monitoring NADH oxidation at 340 nm (ε = 6.22 mM^{-1} cm^{-1}) for 1 h at 37 °C. Second-generation TRAP1 ligands were added immediately before starting recordings.

Cell culture

Mouse sMPNST cells were cultured in Dulbecco's modified Eagle's medium (DMEM; Thermo Fisher Scientific) supplemented with 10% v/v fetal bovine serum (FBS; Thermo Fisher Scientific), 1% v/v L-glutamine (Thermo Fisher Scientific), 1% v/v sodium pyruvate (Thermo Fisher Scientific) and 1% v/v penicillin and streptomycin (Thermo Fisher Scientific) and kept in a 5% CO_2 humidified atmosphere at 37 °C. sMPNST cells were established from $Nf1^{-/-}$; $P53^{-/-}$ skin precursors (SKP)[101] and provided by Dr. Lu Q. Le, University of Texas Southwestern Medical Center, Dallas, TX. Cells were routinely tested for mycoplasma contamination using the MycoAlert® Kit (Lonza).

Generation of TRAP1-knockout cells

TRAP1 knock-out sMPNST cells were generated using CRISPR/Cas9 technique.[102] CRISPR design tool (https://www.crispr.mit.edu) was used to identify the sgRNA sequences against exons 1 and 2 of mouse TRAP1 gene (5′ – CACCGCGCCGAACTCCAGCCAGCGC – 3′ and 5′ – CACCGTTTGTGTGGGGCCCCTAAAC – 3′). Scrambled single guides targeting EGFP were used as negative controls. Sense and antisense oligos for the sgRNAs were cloned into the plasmid lenti-CRISPRv2 (Addgene, #52961) and co-transfected with the packaging plasmids pMDLg/pRRE (Addgene, #12251), pRSV-Rev (Addgene, #12253) and pMD2.G (Addgene, #12259) into human embryonic kidney (HEK) 293 T cells for viral production. Recombinant virus was collected and used to infect sMPNST cells by standard methods. Infected cells were then selected with 1 μg/mL puromycin (Sigma-Aldrich).

Western immunoblots

Total cell lysate was prepared in RIPA buffer (150 mM NaCl, 50 mM Tris-HCl pH 8.0, 1% Nonidet P-40, 0.5% sodium deoxycholate, 0.1% sodium dodecyl sulfate) supplemented with protease and phosphatase inhibitors (Sigma-Aldrich). Protein concentrations were quantified using a BCA Protein Assay Kit (Thermo Fisher Scientific), and 25 μg of total protein lysate was loaded onto 4–12% Bis-Tris NuPage gels (Life Technologies). After proteins were transferred to nitrocellulose Hybond-C Extra membranes (Amersham), levels of TRAP1, SDHA, β-actin and TOM20 were detected with anti rodent TRAP1 (1:1000, Becton Dickinson, #612344), anti SDHA (1:5000, Santa Cruz, #166947) and anti β-actin (1:2500, Santa Cruz, #47778) mouse monoclonal antibodies and anti TOM20 (1:1000, Santa Cruz, #11415) rabbit polyclonal antibody. Protein expression was then acquired with a LICOR Odyssey CLx Imaging System (LI-COR

Biosciences), following incubation with fluorescent IRDye® 680LT goat (polyclonal) anti-mouse (LI-COR Biosciences, #926–68020) or IRDye® 800CW goat (polyclonal) anti-rabbit (LI-COR Biosciences, #926–68021) secondary antibodies.

Measurement of succinate:coenzyme Q reductase (SQR) activity of succinate dehydrogenase (SDH)

To measure the enzymatic activity of SDH, sMPNST cells were collected at 4 °C in a lysis buffer composed by 25 mM potassium phosphate, pH 7.2 (Merck), 5 mM magnesium chloride (Sigma-Aldrich) and phosphatase and protease inhibitors (Sigma-Aldrich). Cell homogenates (40 μg protein per trace) were then incubated for 10 min at 30 °C in a buffer containing 25 mM potassium phosphate, pH 7.2 (Merck), 5 mM magnesium chloride (Sigma-Aldrich), 20 mM sodium succinate (Merck) and 10 μM alamethicin (Sigma-Aldrich). After the incubation time, a mix composed of 5 mM sodium azide (Sigma-Aldrich), 5 μM antimycin A (Calbiochem), 2 μM rotenone (Sigma-Aldrich), 65 μM coenzyme Q1 (Sigma-Aldrich) and 100 μM 2,6-dichloroindophenol (DCPIP, Sigma Aldrich) was added to the medium. Enzymatic activity of SDH was then monitored spectrophotometrically measuring the reduction of DCPIP at 600 nm (ε = 19.1 mM^{-1} cm^{-1}) for 20 min at 30 °C. Each measurement of SDH activity was normalized for protein amount.

In vitro tumorigenesis assays

For focus forming assays, scrambled and TRAP1 knock-out cells were seeded in 12-well plates under standard culture conditions. When cells reached sub-confluence, serum concentration was decreased to 1% and compound **51** was added at the indicated concentration. At the 9th day after serum decrease, foci appeared as thick masses and cells were then washed in PBS (Thermo Fisher Scientific), fixed in methanol (Sigma-Aldrich) for 30 min and stained with GIEMSA solution (Sigma-Aldrich) for 1 h. After washing in PBS to remove excess stain, surface area and foci thickness were analyzed with ImageJ software and combined to obtain the integrated density parameter.

Statistical analysis

Both TRAP1 and Hsp90 activity assays were statistically evaluated with a two-tailed, unpaired Student's *t*-test. SDH activity and focus forming assays were analyzed with one-way analysis of variance (ANOVA), followed by Bonferroni post-hoc test for multiple comparisons. Statistical significance was determined using Origin® 8 (OriginLab). Results with a p-value lower than 0.05 were considered statistically significant; ***$p < 0.001$, **$p < 0.01$, *$p < 0.05$ compared to controls. All analyses consisted of at least three independent experiments and data were displayed as mean ± standard error of the mean (SEM).

CRediT authorship contribution statement. **Alice Triveri:** Methodology, Investigation, Formal analysis. **Carlos Sanchez-Martin:** Methodology, Investigation, Formal analysis. **Luca Torielli:** Methodology, Investigation, Formal analysis. **Stefano A. Serapian:** Methodology, Investigation, Formal analysis. **Filippo Marchetti:** Methodology. **Giovanni D'Acerno:** Methodology. **Valentina Pirota:** Methodology. **Matteo Castelli:** Methodology. **Elisabetta Moroni:** Methodology, Investigation, Formal analysis. **Mariarosaria Ferraro:** Methodology. **Paolo Quadrelli:** Conceptualization, Writing – original draft. **Andrea Rasola:** Conceptualization, Writing – original draft, Funding acquisition, Supervision. **Giorgio Colombo:** Conceptualization, Writing – original draft, Writing – review & editing, Funding acquisition, Supervision.

Acknowledgements

The research leading to these results has received funding from AIRC under IG 2017 - ID. 20019 – P.I. Colombo Giorgio and IG 2017 – ID. 20749 – P.I. Rasola Andrea.

Funding is acknowledged from Children's Tumor Foundation Drug Discovery Initiative Registered Reports 2020-05-001. Luca Torielli is supported by a PhD Fellowship from the "Istituto di Ricerca Pediatrica Città della Speranza". Filippo Marchetti was supported by AIRC through an AIRC-Fellowship.

Declaration of Competing Interest

The authors declare that they have no known competing financial interests or personal relationships that could have appeared to influence the work reported in this paper.

Appendix A. Supplementary data

Supplementary data to this article can be found online at https://doi.org/10.1016/j.jmb.2022.167468.

Received 17 December 2021;
Accepted 21 January 2022;
Available online xxxx

Keywords:
molecular chaperones;
allosteric regulation;
Hsp90;
TRAP1;
protein folding

† These authors gave equal contributions – Co-first authors.

Abbreviations:
MD, Molecular Dynamics; Hsp90, Heat Shock Protein 90 kDa; DF, Distance Fluctuation; NTD, N-Terminal Domain; CTD, C-Terminal Domain

References

1. Monod, J., Wyman, J., Changeux, J.P., (1965). On the nature of allosteric transitions-a plausible model. *J. Mol. Biol.* **12**, 88.
2. Wodak, S.J., Paci, E., Dokholyan, N.V., Berezovsky, I.N., Horovitz, A., Li, J., et al., (2019). Allostery in Its Many Disguises: From Theory to Applications. *Structure (London, England: 1993)* **27**, 566–578.
3. Nussinov, R., Tsai, C.-J., (2013). Allostery in disease and drug discovery. *Cell* **153**, 293–305.
4. Tsai, C.-J., Nussinov, R., (2014). A Unified View of "How Allostery Works". *PLoS Comput. Biol.* **10**, e1003394
5. Papaleo, E., Saladino, G., Lambrughi, M., Lindorff-Larsen, K., Gervasio, F.L., Nussinov, R., (2016). The Role of Protein Loops and Linkers in Conformational Dynamics and Allostery. *Chem. Rev.* **116**, 6391–6423.
6. Szilagyi, A., Nussinov, R., Csermely, P., (2013). Allo-Network Drugs: Extension of the Allosteric Drug Concept to Protein- Protein Interaction and Signaling Networks. *Curr. Top. Med. Chem.* **13**, 64.
7. Zorn, J.A., Wells, J.A., (2010). Turning enzymes ON with small molecules. *Nature Chem. Biol.* **6**, 179–188.
8. Renata, H., Wang, Z.J., Arnold, F.H., (2015). Expanding the Enzyme Universe: Accessing Non-Natural Reactions by Mechanism-Guided Directed Evolution. *Angewandte Chemie-International Edition.* **54**, 3351–3367.
9. Galdadas, I., Qu, S., Oliveira, A.S.F., Olehnovics, E., Mack, A.R., Mojica, M.F., et al., (2021). Allosteric communication in class A β-lactamases occurs via cooperative coupling of loop dynamics. *eLife* **10**, e66567.
10. Galdadas, I., Gervasio, F.L., Cournia, Z., (2020). Unravelling the effect of the E545K mutation on PI3Kα kinase. *Chem. Sci.* **11**, 3511–3515.
11. Kumar Mv, V., Ebna Noor, R., Davis, R.E., Zhang, Z., Sipavicius, E., Keramisanou, D., et al., (2018). Molecular insights into the interaction of Hsp90 with allosteric inhibitors targeting the C-terminal domain. *MedChemComm.*.
12. Pricer, R., Gestwicki, J.E., Mapp, A.K., (2017). From Fuzzy to Function: The New Frontier of Protein-Protein Interactions. *Acc. Chem. Res.* **50**, 584–589.
13. Gestwicki, J.E., Shao, H., (2019). Inhibitors and chemical probes for molecular chaperone networks. *J. Biol. Chem.* **294**, 2151–2161.
14. Wang, T., Rodina, A., Dunphy, M.P., Corben, A., Modi, S., Guzman, M.L., et al., (2019). Chaperome heterogeneity and its implications for cancer study and treatment. *J. Biol. Chem.* **294**, 2162–2179.
15. Jeong, H., Mason, S.P., Barabási, A.L., Oltvai, Z.N., (2001). Lethality and centrality in protein networks. *Nature* **411**, 41–42.
16. Pillarsetty, N., Jhaveri, K., Taldone, T., Caldas-Lopes, E., Punzalan, B., Joshi, S., et al., (2019). Paradigms for Precision Medicine in Epichaperome Cancer Therapy. *Cancer Cell* **36** 559-73.e7.
17. Backe, S.J., Sager, R.A., Woodford, M.R., Makedon, A. M., Mollapour, M., (2020). Post-translational modifications of Hsp90 and translating the chaperone code. *J. Biol. Chem.* **295**, 11099–11117.
18. Altieri, D.C., Languino, L.R., Lian, J.B., Stein, J.L., Leav, I., van Wijnen, A.J., et al., (2009). Prostate Cancer Regulatory Networks. *J. Cell. Biochem.* **107**, 845–852.
19. Kang, B.H., Plescia, J., Song, H.Y., Meli, M., Colombo, G., Beebe, K., et al., (2009). Combinatorial drug design targeting multiple cancer signaling networks controlled by mitochondrial Hsp90. *J. Clin. Invest.* **119**, 454–464.
20. Altieri, D.C., (2006). Targeted therapy by disabling crossroad signaling networks: the survivin paradigm. *Mol. Cancer Ther.* **5**, 478–482.
21. Agarwal, E., Altman Brian, J., Ho Seo, J., Bertolini, I., Ghosh Jagadish, C., Kaur, A., et al. Myc Regulation of a Mitochondrial Trafficking Network Mediates Tumor Cell Invasion and Metastasis. Mol. Cell. Biol. 39, e00109-19. DOI: 10.1128/MCB.00109-19.
22. Vogelstein, B., Kinzler, K.W., (2004). Cancer genes and the pathways they control. *Nat Medicine.* **10**, 788–789.
23. Schopf, F.H., Biebl, M.M., Buchner, J., (2017). The HSP90 chaperone machinery. *Nature Rev. Mol. Cell Biol.* **18**, 345–360.
24. Krukenberg, K.A., Street, T.O., Lavery, L.A., Agard, D.A., (2011). Conformational dynamics of the molecular chaperone Hsp90. *Q. Rev. Biophys.* **44**, 229–255.
25. Walton-Diaz, A., Khan, S., Bourboulia, D., Trepel, J.B., Neckers, L., Mollapour, M., (2013). Contributions of co-chaperones and post-translational modifications towards Hsp90 drug sensitivity. *Future Med. Chem.* **5**, 1059–1071.
26. Verba, K.A., Agard, D.A., (2017). How Hsp90 and Cdc37 Lubricate Kinase Molecular Switches. *Trends Biochem. Sci.* **42**, 799–811.
27. Lavery, L.A., Partridge, J.R., Ramelot, T.A., Elnatan, D., Kennedy, M.A., Agard, D.A., (2014). Structural asimmetry in the closed state of mitochondrial Hsp90 (TRAP1) supports a two-step ATP hydrolysis mechanism. *Mol. Cell* **53**, 330–343.
28. Genest, O., Reidy, M., Street, T.O., Hoskins, J.R., Camberg, J.L., Agard, D.A., et al., (2013). Uncovering a region of heat shock protein 90 important for client binding in E. coli and chaperone function in yeast. *Mol. Cell* **49**, 464–473.
29. Elnatan, D., Betegon, M., Liu, Y., Ramelot, T., Kennedy, M.A., Agard, D.A., (2017). Symmetry broken and rebroken during the ATP hydrolysis cycle of the mitochondrial Hsp90 TRAP1. *eLife* **6**, e25235.
30. Johnson, J.L., (2012). Evolution and function of diverse Hsp90 homologs and cochaperone proteins. *Biochim. Biophys. Acta, Mol. Cell. Biol. Lipids* **1823**, 607–613.
31. Patel, P.D., Chiosis, G., (2013). Paralog-selective Hsp90 inhibitors define tumor-specific regulation of HER2. *Nature Chem. Biol.* **9**, 677–684.

32. Mishra, S.J., Khandelwal, A., Banerjee, M., Balch, M., Peng, S., Davis, R.E., et al., (2021). Selective Inhibition of the Hsp90α Isoform. *Angew. Chem. Int. Ed.* **60**, 10547–10551.
33. Serapian, S.A., Sanchez-Martín, C., Moroni, E., Rasola, A., Colombo, G., (2021). Targeting the mitochondrial chaperone TRAP1: strategies and therapeutic perspectives. *Trends Pharmacol. Sci.*.
34. D'Annessa, I., Raniolo, S., Limongelli, V., Di Marino, D., Colombo, G., (2019). Ligand Binding, Unbinding, and Allosteric Effects: Deciphering Small-Molecule Modulation of HSP90. *J. Chem. Theory Comput.* **15**, 6368–6381.
35. Paladino, A., Woodford, M.R., Backe, S.J., Sager, R.A., Kancherla, P., Daneshvar, M.A., et al., (2020). Chemical Perturbation of Oncogenic Protein Folding: from the Prediction of Locally Unstable Structures to the Design of Disruptors of Hsp90–Client Interactions. *Chemistry – A Eur. J.* **26**, 9459–9465.
36. Sanchez-Martin, C., Moroni, E., Ferraro, M., Laquatra, C., Cannino, G., Masgras, I., et al., (2020). Rational Design of Allosteric and Selective Inhibitors of the Molecular Chaperone TRAP1. *Cell Reports* **31**, 107531
37. Forsberg, L.K., Liu, W., Holzbeierlein, J., Blagg, B.S.J., (2017). Modified biphenyl Hsp90 C-terminal inhibitors for the treatment of cancer. *Bioorg. Med. Chem. Letters* **27**, 4514–4519.
38. Forsberg, L.K., Anyika, M., You, Z., Emery, S., McMullen, M., Dobrowsky, R.T., et al., (2018). Development of noviomimetics that modulate molecular chaperones and manifest neuroprotective effects. *Eur. J. Med. Chem.* **143**, 1428–1435.
39. Neckers, L., Blagg, B., Haystead, T., Trepel, J.B., Whitesell, L., Picard, D., (2018). Methods to validate Hsp90 inhibitor specificity, to identify off-target effects, and to rethink approaches for further clinical development. *Cell Stress Chaperones*.
40. Daura, X. (2019). Advances in the Computational Identification of Allosteric Sites and Pathways in Proteins. In: Zhang, J., Nussinov, R. (Eds.), Protein Allostery in Drug Discovery: Springer Nature .
41. Panjkovich, A., Daura, X., (2010). Assessing the structural conservation of protein pockets to study functional and allosteric sites: implications for drug discovery. *BMC Struct. Biol.* **10**, 9.
42. Panjkovich, A., Daura, X., (2012). Exploiting protein flexibility to predict the location of allosteric sites. *BMC Bioinf.* **13**, 273.
43. Malmstrom, R.D., Kornev, A.P., Taylor, S.S., Amaro, R. E., (2015). Allostery through the computational microscope: cAMP activation of a canonical signalling domain. *Nature Commun.* **6**, 7588.
44. Wagner, J.R., Lee, C.T., Durrant, J.D., Malmstrom, R.D., Feher, V.A., Amaro, R.E., (2016). Emerging Computational Methods for the Rational Discovery of Allosteric Drugs. *Chem. Rev.* **116**, 6370–6390.
45. Zhao, H.P., Donnelly, A.C., Kusuma, B.R., Brandt, G.E.L., Brown, D., Rajewski, R.A., et al., (2011). Engineering an Antibiotic to Fight Cancer: Optimization of the Novobiocin Scaffold to Produce Anti-proliferative Agents. *J. Med. Chem.* **54**, 3839–3853.
46. Moroni, E., Zhao, H., Blagg, B.S., Colombo, G., (2014). Exploiting Conformational Dynamics in Drug Discovery: Design of C-Terminal Inhibitors of Hsp90 with Improved Activities. *J. Chem.Inf Model.*. PMID: 24397468.
47. Zhao, H., Moroni, E., Colombo, G., Blagg, B.S., (2014). Identification of a New Scaffold for Hsp90 C-Terminal Inhibition. *ACS Med. Chem. Letters* **5**, 84–88.
48. Ma, J., Pan, P., Anyika, M., Blagg, B.S.J., Dobrowsky, R. T., (2015). Modulating molecular chaperones improves mitochondrial bioenergetics and decreases the inflammatory transcriptome in diabetic sensory neurons. *ACS Chem. Neurosci.* **6**, 1637–1648.
49. Zhao, H., Garg, G., Zhao, J., Moroni, E., Girgis, A., Franco, L.S., et al., (2015). Design, synthesis and biological evaluation of biphenylamide derivatives as Hsp90 C-terminal inhibitors. *Eur. J. Med. Chem.* **89**, 442–466.
50. Sanchez-Martin, C., Serapian, S.A., Colombo, G., Rasola, A., (2020). Dynamically Shaping Chaperones Allosteric Modulators of HSP90 Family as Regulatory Tools of Cell Metabolism in Neoplastic Progression. *Front. Oncol.* **10**, 1177.
51. Rasola, A., Neckers, L., Picard, D., (2014). Mitochondrial oxidative phosphorylation TRAP(1)ped in tumor cells. *Trends Cell Biol.* **24**, 455–463.
52. Masgras, I., Sanchez-Martin, C., Colombo, G., Rasola, A., (2017). The Chaperone TRAP1 As a Modulator of the Mitochondrial Adaptations in Cancer Cells. *Front. Oncol.* **7**
53. Kowalik, M.A., Guzzo, G., Morandi, A., Perra, A., Menegon, S., Masgras, I., et al., (2016). Metabolic reprogramming discriminates aggressive vs. slowly growing preneoplastic lesions at early stages of HCC development. *Cancer Res.* **76**
54. Yoshida, S., Tsutsumi, S., Muhlebach, G., Sourbier, C., Lee, M.-J., Lee, S., et al., (2013). Molecular chaperone TRAP1 regulates a metabolic switch between mitochondrial respiration and aerobic glycolysis. *Proc. Natl. Acad. Sci.*. 201220659.
55. Si, T., Yang, G., Qiu, X., Luo, Y., Liu, B., Wang, B., (2015). Expression of tumor necrosis factor receptor-associated protein 1 and its clinical significance in kidney cancer. *Int. J. Clin. Exp. Pathol.* **8**, 13090–13095.
56. Moroni, E., Agard, D.A., Colombo, G., (2018). The Structural Asymmetry of Mitochondrial Hsp90 (Trap1) Determines Fine Tuning of Functional Dynamics. *J. Chem. Theory Comput.* **14**, 1033–1044.
57. Amadei, A., Linssen, A.B.M., Berendsen, H.J.C., (1993). Essential dynamics of proteins. *Proteins Struct. Funct. Genet.* **17**, 412–425.
58. Morra, G., Potestio, R., Micheletti, C., Colombo, G., (2012). Corresponding Functional Dynamics across the Hsp90 Chaperone Family: Insights from a Multiscale Analysis of MD Simulations. *PLoS Comput. Biol.* **8**, e1002433
59. Corrada, D., Morra, G., Colombo, G., (2013). Investigating Allostery in Molecular Recognition: Insights from a Computational Study of Multiple Antibody-Antigen Complexes. *J. Phys. Chem. B* **117**, 535–552.
60. Paladino, A., Morra, G., Colombo, G., (2015). Structural Stability and Flexibility Direct the Selection of Activating Mutations in Epidermal Growth Factor Receptor Kinase. *J. Chem. Inf. Model.* **55**, 1377–1387.
61. Rehn, A., Moroni, E., Zierer, B.K., Tippel, F., Morra, G., John, C., et al., (2016). Allosteric Regulation Points Control the Conformational Dynamics of the Molecular Chaperone Hsp90. *J. Mol. Biol.* **428**, 4559–4571.
62. D'Annessa, I., Moroni, E., Colombo, G., (2021). Visualizing the Dynamics of a Protein Folding

Machinery: The Mechanism of Asymmetric ATP Processing in Hsp90 and its Implications for Client Remodelling. *J. Mol. Biol.* **433**
63. Serapian, S.A., Moroni, E., Ferraro, M., Colombo, G., (2021). Atomistic Simulations of the Mechanisms of the Poorly Catalytic Mitochondrial Chaperone Trap 1: Insights into the Effects of Structural Asymmetry on Reactivity. *ACS Catal.* **11**, 8605–8620.
64. Serapian, S.A., van der Kamp, M.W., (2019). Unpicking the Cause of Stereoselectivity in Actinorhodin Ketoreductase Variants with Atomistic Simulations. *ACS Catal.* **9**, 2381–2394.
65. Chiosis, G., (2016). Heat Shock Proteins in Disease - From Molecular Mechanisms to Therapeutics. *Curr. Top. Med. Chem.* **16**, 2727–2728.
66. Shrestha, L., Patel, H.J., Chiosis, G., (2016). Chemical Tools to Investigate Mechanisms Associated with HSP90 and HSP70 in Disease. *Cell Chem. Biol.* **23**, 158–172.
67. Maestro, 2019. Schrödinger Release 2019-2: Maestro. Schrödinger, LLC, New York, NY.
68. Frey, S., Leskovar, A., Reinstein, J., Buchner, K., (2007). The ATPase cycle of the endoplasmic chaperone Grp94. *J. Biol. Chem.* **282**, 35612–35620.
69. Sciacovelli, M., Guzzo, G., Morello, V., Frezza, C., Zheng, L., Nannini, N., et al., (2013). The Mitochondrial Chaperone TRAP1 Promotes Neoplastic Growth by Inhibiting Succinate Dehydrogenase. *Cell Metab.* **17**, 988–999.
70. Guzzo, G., Sciacovelli, M., Bernardi, P., Rasola, A., (2014). Inhibition of succinate dehydrogenase by the mitochondrial chaperone TRAP1 has anti-oxidant and anti-apoptotic effects on tumor cells. *Oncotarget.* **5**, 11897–11908.
71. Masgras, I., Ciscato, F., Brunati, A.M., Tibaldi, E., Indraccolo, S., Curtarello, M., et al., (2017). Absence of Neurofibromin Induces an Oncogenic Metabolic Switch via Mitochondrial ERK-Mediated Phosphorylation of the Chaperone TRAP1. *Cell Reports* **18**, 659–672.
72. Sanchez-Martin, C., Menon, D., Moroni, E., Ferraro, M., Masgras, I., Elsey, J., et al., (2021). Honokiol Bis-Dichloroacetate Is a Selective Allosteric Inhibitor of the Mitochondrial Chaperone TRAP1. *Antioxid. Redox Signal.* **34**, 505–516.
73. Khandelwal, A., Kent, C.N., Balch, M., Peng, S., Mishra, S.J., Deng, J., et al., (2018). Structure-guided design of an Hsp90β N-terminal isoform-selective inhibitor. *Nature Commun.* **9**, 425.
74. Huck, J.D., Que, N.L.S., Sharma, S., Taldone, T., Chiosis, G., Gewirth, D.T., (2019). Structures of Hsp90α and Hsp90β bound to a purine-scaffold inhibitor reveal an exploitable residue for drug selectivity. *Proteins Struct. Funct. Bioinf.* **87**, 869–877.
75. Taldone, T., Wang, T., Rodina, A., Pillarsetty, N.V.K., Digwal, C.S., Sharma, S., et al., (2020). A chemical biology approach to the chaperome in cancer—HSP90 and beyond. *Cold Spring Harbor Perspect. Biol.* **12**
76. Que, N.L.S., Crowley, V.M., Duerfeldt, A.S., Zhao, J., Kent, C.N., Blagg, B.S.J., et al., (2018). Structure Based Design of a Grp94-Selective Inhibitor: Exploiting a Key Residue in Grp94 To Optimize Paralog-Selective Binding. *J. Med. Chem.* **61**, 2793–2805.
77. Lee, C., Park, H.-K., Jeong, H., Lim, J., Lee, A.-J., Cheon, K.Y., et al., (2015). Development of a Mitochondria-Targeted Hsp90 Inhibitor Based on the Crystal Structures of Human TRAP1. *J. Am. Chem. Soc.* **137**, 4358–4367.
78. Hu, S., Ferraro, M., Thomas, A.P., Chung, J.M., Yoon, N. G., Seol, J.-H., et al., (2020). Dual Binding to Orthosteric and Allosteric Sites Enhances the Anticancer Activity of a TRAP1-Targeting Drug. *J. Med. Chem.* **63**, 2930–2940.
79. Ferraro, M., Moroni, E., Ippoliti, E., Rinaldi, S., Sanchez-Martin, C., Rasola, A., et al., (2021). Machine Learning of Allosteric Effects: The Analysis of Ligand-Induced Dynamics to Predict Functional Effects in TRAP1. *J. Phys. Chem. B* **125**, 101–114.
80. Marchetti, F., Moroni, E., Pandini, A., Colombo, G., (2021). Machine Learning Prediction of Allosteric Drug Activity from Molecular Dynamics. *J. Phys. Chem. Letters* **12**, 3724–3732.
81. Miyata, Y., Li, X., Lee, H.F., Jinwal, U.K., Srinivasan, S.R., Seguin, S.P., et al., (2013). Synthesis and initial evaluation of YM-08, a blood-brain barrier permeable derivative of the heat shock protein 70 (Hsp70) inhibitor MKT-077, which reduces tau levels. *ACS Chem. Neurosci.* **4**, 930–939.
82. Lavery Laura, A., Partridge James, R., Ramelot Theresa, A., Elnatan, D., Kennedy Michael, A., Agard, D.A., (2014). Structural Asymmetry in the Closed State of Mitochondrial Hsp90 (TRAP1) Supports a Two-Step ATP Hydrolysis Mechanism. *Mol. Cell* **53**, 330–343.
83. Case, D.A., Cheatham Iii, T.E., Darden, T., Gohlke, H., Luo, R., Merz Jr, K.M., et al., (2005). The Amber biomolecular simulation programs. *J. Comput. Chem.* **26**, 1668–1688.
84. Maier, J.A., Martinez, C., Kasavajhala, K., Wickstrom, L., Hauser, K.E., Simmerling, C., (2015). ff14SB: Improving the Accuracy of Protein Side Chain and Backbone Parameters from ff99SB. *J. Chem. Theory Comput.* **11**, 3696–3713.
85. Meagher, K.L., Redman, L.T., Carlson, H.A., (2003). Development of polyphosphate parameters for use with the AMBER force field. *J. Comput. Chem.* **24**, 1016–1025.
86. Allnér, O., Nilsson, L., Villa, A., (2012). Magnesium Ion-Water Coordination and Exchange in Biomolecular Simulations. *J. Chem. Theory Comput.* **8**, 1493–1502.
87. Jorgensen, W.L., Chandrasekhar, J., Madura, J., Impey, R.W., Klein, M.L., (1983). Comparison of simple potential functions for simulating liquid water. *J. Chem. Phys.* **79**, 926–935.
88. Joung, I.S., Cheatham, T.E., (2008). Determination of Alkali and Halide Monovalent Ion Parameters for Use in Explicitly Solvated Biomolecular Simulations. *J. Phys. Chem. B* **112**, 9020–9041.
89. Wang, J., Wolf, R.M., Caldwell, J.W., Kollman, P.A., Case, D.A., (2004). Development and testing of a general amber force field. *J. Comput. Chem.* **25**, 1157–1174.
90. Frisch, M.J., Trucks, G.W., Schlegel, H.B., Scuseria, G. E., Robb, M.A., Cheeseman, J.R., et al. Gaussian 09, Revision B.01. Gaussian 09, Revision B01, Gaussian, Inc, Wallingford CT2009.
91. Lee, C., Yang, W., Parr, R.G., (1988). Development of the Colle-Salvetti correlation-energy formula into a functional of the electron density. *Phys. Rev. B* **37**, 785–789.
92. Bayly, C.I., Cieplak, P., Cornell, W., Kollman, P.A., (1993). A well-behaved electrostatic potential based method using charge restraints for deriving atomic charges: the RESP model. *J. Phys. Chem.*. **97**, 10269–10280.

93. Case, D.A., Cerutti, D.S., Cheatham, T.E.I., Darden, T.A., Duke, R.E., Giese, T.J., et al., (2018). AMBER 2018. University of California, San Francisco.
94. Salomon-Ferrer, R., Götz, A.W., Poole, D., Le Grand, S., Walker, R.C., (2013). Routine Microsecond Molecular Dynamics Simulations with AMBER on GPUs. 2. Explicit Solvent Particle Mesh Ewald. *J. Chem. Theory Comput.* **9**, 3878–3888.
95. Miyamoto, S., Kollman, P.A., (1992). SETTLE: An analytical version of the SHAKE and RATTLE algorithms for rigid water models. *J Comp Chem.* **13**, 952–962.
96. Darden, T., York, D., Pedersen, L., (1993). Particle mesh Ewald: An N-log(N) method for Ewald sums in large systems. *J. Chem. Phys.* **98**
97. Berendsen, H.J.C., Postma, J.P.M., van Gunsteren, W.F., Di Nola, A., Haak, J.R., (1984). Molecular dynamics with coupling to an external bath. *J. Chem. Phys.* **81**, 3684–3690.
98. Sokal, R.R., (1958). A statistical method for evaluating systematic relationship. *University of Kansas Sci. Bull.* **28**, 1409–1438.
99. Halgren, T.A., (2009). Identifying and Characterizing Binding Sites and Assessing Druggability. *J. Chem. Inf Model.* **49**, 377.
100. Leskovar, A., Wegele, H., Werbeck, N.D., Buchner, J., Reinstein, J., (2008). The ATPase Cycle of the Mitochondrial Hsp90 Analog Trap1*. *J. Biol. Chem.* **283**, 11677–11688.
101. Mo, W., Chen, J., Patel, A., Zhang, L., Chau, V., Li, Y., et al., (2013). CXCR4/CXCL12 mediate autocrine cell-cycle progression in NF1-associated malignant peripheral nerve sheath tumors. *Cell* **152**, 1077–1090.
102. Shalem, O., Sanjana, N.E., Hartenian, E., Shi, X., Scott, D.A., Mikkelson, T., et al., (2014). Genome-scale CRISPR-Cas9 knockout screening in human cells. *Science (New York, NY).* **343**, 84–87.